

# Global aerosol typing classification using a new hybrid algorithm utilizing Aerosol Robotic Network data

Xiaoli Wei<sup>1</sup>, Qian Cui<sup>5</sup>, Leiming Ma<sup>1</sup>, Feng Zhang<sup>2,3</sup>, Wenwen Li<sup>2,3</sup>, Peng Liu<sup>4</sup>

<sup>1</sup> Shanghai Meteorological Service 200030, China;

<sup>2</sup> Shanghai Qi Zhi Institute, Shanghai, 200232, China;

<sup>3</sup> Department of Atmospheric and Oceanic Sciences & Institute of Atmospheric Sciences, Fudan University, Shanghai, 200438, China;

<sup>4</sup> School of Atmospheric Science, Nanjing University of Information Science and Technology, Nanjing 210044, China;

<sup>5</sup> Caidian Meteorological Service, Wuhan, 430000, China

Correspondence to: Feng Zhang (fengzhang@fudan.edu.cn)

## Abstract

Aerosols have great uncertainty owing to the complex changes in their composition in different regions. The radiation properties of different aerosol types differ considerably and are vital in studying aerosol regional and/or global climate effects. Traditional aerosol-type identification algorithms, generally based on cluster or empirical analysis methods, are often inaccurate and time-consuming. In response, our study Hence, we aimed to develop a new aerosol-type classification model using an innovative hybrid algorithm to improve the precision and efficiency of aerosol-type identification. This novel algorithm incorporates an optical database, constructed using the Mie scattering model, and employs a random forest algorithm to classify different aerosol types based on the optical data from the database. The complex refractive index was used as a baseline to assess the performance of our hybrid algorithm against the traditional Gaussian kernel density clustering method for aerosol type identification. An optical database was built using Mie scattering and a complex refractive index was used as a baseline to identify different aerosol types by applying a random forest algorithm to train the aerosol optical parameters obtained from the Aerosol Robotic Network sites. The hybrid algorithm demonstrated impressive consistency rates of ~~The consistency rates of the new model with the traditional Gaussian were~~ 90%, 85%, 84%, 84%, and 100% for dust, mixed-coarse, mixed-fine,

31 urban/industrial, and biomass burning aerosols, respectively. Moreover, it achieved  
32 remarkable precision, with F-score and accuracy scores of ~~The corresponding~~  
33 ~~precision of the new hybrid algorithm (F-score and accuracy scores) was~~ 95%, 89%,  
34 91%, and 89%. Lastly, a global map of aerosol types was generated using the new  
35 model to characterize aerosol types across the five continents. This study utilizing a  
36 novel approach for the classification of aerosol will help improve the accuracy of  
37 aerosol inversion and determine the sources of aerosol pollution.

38 **Keywords:** Aerosol typing classification, Hybrid algorithm, Complex refractive index,  
39 AERONET

## 40 **1. Introduction**

41 Atmospheric aerosols are tiny solid or liquid particles suspended in the  
42 atmosphere. Aerosols indirectly affect the energy budget and water cycle of the earth's  
43 gas system by absorbing and scattering solar radiation or by changing the optical  
44 properties and life cycle of the cloud as condensation nuclei of cloud droplets  
45 (Redemann et al. 2000; Ramanathan et al. 2001). Additionally, desert dust, biomass  
46 smog, and anthropogenic emissions of air pollutants can affect visibility, air quality,  
47 and human health (Hess et al., 1998; Tong et al., 2017; Siomos et al., 2020).  
48 Evaluating the impact of aerosols on radiative transfer is complex, primarily because  
49 of the uncertainty of radiative forcing caused by the high spatiotemporal dynamic  
50 variation of aerosol optical and physical characteristics in different regions  
51 (Kaskaoutis et al., 2011; Che et al., 2018; Elham et al., 2023). The aerosol type  
52 embodies the long-term average physicochemical properties of aerosols in a certain  
53 area (Kiehl & Briegleb, 1993; Lu et al., 2023). Therefore, accurate identification of  
54 aerosol types can drive the study of the climatic effects of aerosols, tracking and  
55 control of environmental pollution sources, and precision of radiation transmission  
56 models.

57 Aerosol types are defined based on the radiation properties of different types of  
58 aerosol particles owing to the large variation in their optical, physical, and chemical

59 properties. Currently, aerosol types are classified by two ways using two different  
60 clustering techniques (Kumar et al., 2018). First, based on different sources and  
61 properties at different observation points worldwide, aerosols are classified as follows:  
62 dust aerosols from deserts, biomass combustion aerosols from forests or grasslands,  
63 and urban/industrial (U/I) aerosols from fuel combustion in densely populated urban  
64 areas (Dubovik et al., 2002; Pawar et al., 2015; Yousefi et al., 2020). Second, based on  
65 the size of the radiation absorption rate, aerosols into four categories: carbonaceous  
66 (fine-absorbing mode), soil dust (coarse absorption mode), sulfates (nonabsorbing  
67 fine-grained mode), and sea salt aerosols (nonabsorbing coarse-grained mode) (Kim  
68 et al., 2007; Levy et al., 2007). The second one is a type of subcategorize  
69 anthropogenic aerosol. The first one is commonly used for aerosol retrieval. Therefore,  
70 the first aerosol type classification is more common in research. The optical properties  
71 of aerosols observed at ground stations are commonly used to construct a two-  
72 dimensional identification space to obtain the aerosol types by clustering techniques.  
73 Many combinations of optical properties and parameters are available; They include  
74  $EAE_{440-870nm}$  (extinction angstrom exponent) vs.  $SSA_{440nm}$  (single-scattering albedo),  
75  $AAE_{440-870nm}$  (absorption angstrom exponent) vs.  $EAE_{440-870nm}$ ,  $AAE_{440-870nm}$  vs.  
76  $FMF_{550nm}$  (fine mode fraction), and  $SSA_{440nm}$  vs.  $EAE_{440-870nm}$  (Lee et al., 2010; Shin et  
77 al., 2019; Choi, et al., 2021). Studies have highlighted the importance of selecting  
78 appropriate aerosol properties for accurate aerosol type identification (Giles et al.,  
79 2012; Che et al., 2018).

80 Among the aerosol-type classification methodologies developed, those using  
81 threshold and empirical analyses have the greatest potential for large-area and fixed-  
82 period applications (Eck et al., 1999; Omar et al., 2005; Yang et al., 2009).  
83 Traditionally, the aerosol-type classification algorithm mainly distinguishes different  
84 aerosol types based on their optical properties and determines the threshold of their  
85 optical properties based on clustering. However, the composition of aerosols changes  
86 rapidly with time and location, owing to the combined influence of natural conditions  
87 and human activities (for example, tornadoes and various anthropogenic activities)  
88 (Sheridan et al., 2001). Unfortunately, determining aerosol types accurately and

89 rapidly is a challenge when using traditional methods (Bahadur et al., 2012;Shin et al.,  
90 2019;Lin et al., 2021). Nevertheless, with advancements in data science, artificial  
91 intelligence techniques have aided the accurate and rapid recognition of different  
92 aerosol types.

93 Artificial intelligence algorithms can receive multiple aerosol characteristic  
94 parameters as input, thus preventing the sole reliance of aerosol classification on a  
95 limited number of features (Li et al., 2022; Wang et al., 2023). For example, Boselli  
96 (2012) performed a k-means clustering analysis of single scattering albedo (SSA),  
97 aerosol optical depth (AOD), electrical asymmetry effect (EAE), and asymmetry  
98 parameter (g) datasets for the central Mediterranean Sea for the classification of  
99 aerosol into four: dusty, continental, oceanic, or mixed aerosols. Nicolae (2018)  
100 developed a neural network algorithm to estimate the aerosol typing of Lidar data and  
101 Hamill (2016) introduced the Mahalanobis Distance for aerosol classification to  
102 determine a specific aerosol type for each reference cluster. Li (2022) generated  
103 spatial contiguous aerosol type map in China with an empirical aerosol type retrieval  
104 algorithm. Overall, limited information on the optical properties of aerosols can  
105 reasonably determine the type of aerosol (Hamill et al., 2016). However, some  
106 challenges remain in identifying aerosol types through machine learning. First, the  
107 amount of valid ground aerosol property data that can be used for training is less due  
108 to cloud removal and quality control. Second, the accuracy of machine learning  
109 depends on the labeled aerosol typing dataset, and finding a suitable classification  
110 method to classify the dataset is challenging. Third, evaluating the accuracy of the  
111 final trained model is also tedious (Zhang & Li, 2019;Siomos et al., 2020; Choi, et al.,  
112 2021a,b)

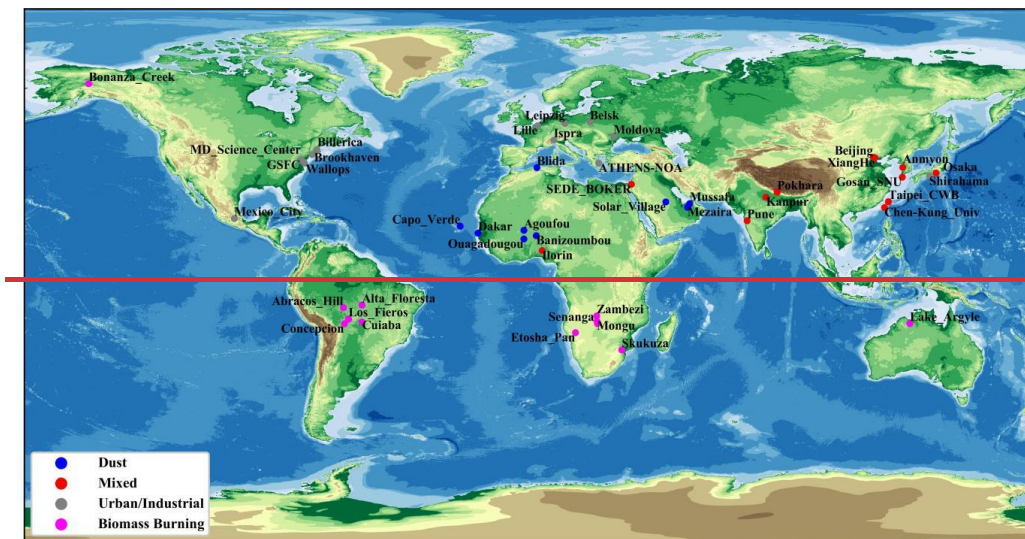
113 The traditional aerosol type identification methods are easily limited by time and  
114 space, and most of them only classify aerosol types using two optical property  
115 parameters, limiting the complete characterization of aerosols. Considering these  
116 limitations, we aimed to (1) develop a new algorithm that can accurately and quickly  
117 identify aerosol types to overcome existing problems such as low accuracy,  
118 insufficient data, and difficulty in setting labels; (2) investigate the characteristics of

119 the regional spatial distribution of global aerosol types obtained using the new  
120 machine learning algorithms, considering the large regional differences in aerosol  
121 types. To achieve this, we propose a new aerosol-type classification algorithm based  
122 on a Gaussian cluster and random forest algorithm to generate an aerosol-typing map  
123 over several representative regions of the world.

## 124 **2. Study area and data**

125 Figure 1 illustrates the research area and the distribution of the Aerosol Robotic  
126 Network (AERONET) sites, strategically encompassing major global regions to  
127 validate the universality of the research algorithm. The study utilized 47 marked  
128 aerosol sites across five continents, leveraging them to train and validate the machine  
129 learning approach based on a comprehensive literature review. Figure 1 shows the  
130 study area and the Aerosol Robotic Network (AERONET) site distribution, which  
131 covers major regions of the world, to ensure the generalizability of the research  
132 algorithm. We used 47 aerosol sites as marked on the map that were distributed over  
133 five continents to train and verify machine learning by literature review. The 47 sites  
134 represent different aerosol-type properties of different aerosol source regions,  
135 including dust, mixed (mixed coarse and mixed fine aerosols), U/I, and biomass  
136 burning (BB) aerosols (Table 1 and Figure 1). Marine aerosols were not considered  
137 because their low optical thickness values (generally  $<0.4$ ) can result in a less valid  
138 data scale that would not meet the study requirements. Here, the aerosol source region  
139 refers to the area affected by one dominant emission source, where the aerosol types  
140 are fixed and not easily confused (Giles et al., 2012; Hamill et al., 2016). Table 2  
141 presents the optical properties and microphysical characteristic parameters of aerosols  
142 at four bands of AERONET (440, 675, 870, and 1020 nm). These parameters were  
143 used to construct a database of SSA, AOD, and asymmetry parameters. Further,  
144 typical sites dominated by different aerosol types worldwide were selected for  
145 compositional analysis using the new model. The selected sites are distributed across  
146 different regions of the world and represent a specific aerosol-dominated type and  
147 aerosol source region.

148 For dust aerosols, five AERONET sites, namely Banizoumbou, Capo Verde,  
 149 Dakar, and Ouagadougou in Africa and Solar-Solar Village in West Asia, influenced  
 150 by the Saharan Desert, were considered. The Dakar and Cape-Capo Verde sites are  
 151 located at the tip of the CapeCapo Verde Peninsula—the westernmost part of Africa,  
 152 bordering the Atlantic Ocean. Although these two sites are located in the ocean, they  
 153 are dominated by dust aerosols influenced by aerosol plumes in the Saharan Desert.  
 154 Moreover, the Banizoumbou and Ouagadougou sites are in the middle of Africa. Here,  
 155 the northeasterly winds prevail in winter, and northwesterly winds prevail in summer,  
 156 which can bring dust aerosols from the Saharan Desert. For mixed aerosols, the  
 157 AERONET sites Ilorin, Kanpur, Sede\_Boker, and XiangHe were selected. For U/I  
 158 aerosols, the AERONET sites GSFC, Ispra, Mexico\_City, and Moldova were selected.  
 159 Four AERONET sites, namely, Alta\_Floresta, Abracos\_Hill, Lake\_Argyle, and  
 160 Mongu, were selected as BB aerosol-dominant sites.



161



162

163 **Figure 1.** Study area and 47 AERONET sites selected by literature review.

164 **Table 1.** 47 AERONET sites selected by literature review.

Aerosol Type	Sites for Training	Sites for Testing
Dust	Agoufou,Capo_Verde,Dakar,-Mezaira, Mussafa,-Ouagadougou	Banizoumbou, Solar_Village, Blida
Mixed	Anmyon, Beijing, Chen-Kung_Univ, Ilorin, Kanpur, Sede_Boker, Gosan_SUN, Pune, Taipei_CWB	Osaka, XiangHe, Pokhara
Urban/Industry	Brookhaven,Billerica,Belsk,GSFC,Ispra,UMBC,Lille, Mexcio_City,Moldova,MD_Science_Center,Wallops	Athens_Noa,Shirahama, Leipzig
Biomass Burning	Abracos_Hill,Alta_Floresta,Cuiaba,Concepcion Los_Fieros,Mongu,Senanga,-Skukuza,Zambezi	Bonanza_Creek, Etosha_Pan, Lake_Argyle

165 **Table 2.** The optical and microphysical properties for aerosol type identification.

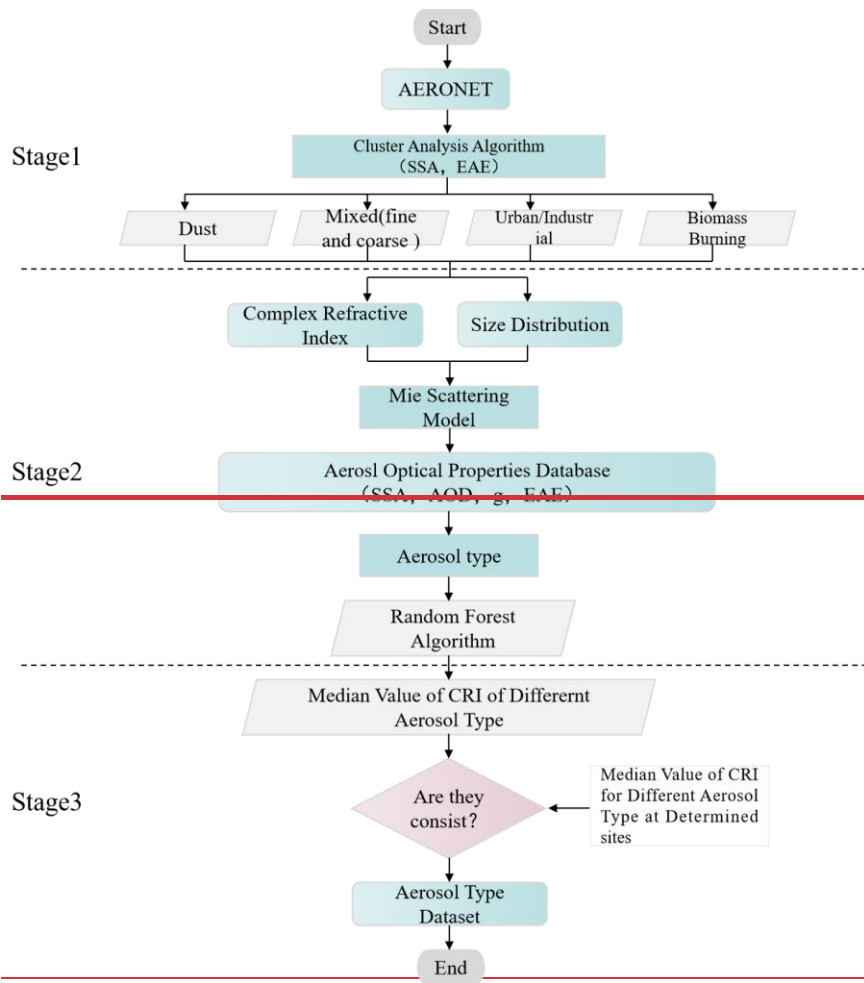
	Parameters	Variables (band waves)
Optical Properties	Ångström Exponent (AE)	EAE (440-870) <sup>1</sup>
	Aerosol Optical Depth (AOD)	AOD (440,675,870,1020) <sup>1</sup>
	Single Scattering Albedo (SSA)	SSA (440,675,870,1020) <sup>1</sup>
	Asymmetry Parameter	g (440,675,870,1020) <sup>1</sup>
	Imaginary Part of the Complex Refractive Index	REFI (440,675,870,1020) <sup>1</sup>
	Real Part of the Complex Refractive Index	REFR(440,675,870,1020) <sup>1</sup>
Microphysical Properties	Effective Radius	EffRad-F <sup>2</sup> , EffRad-C <sup>2</sup>
	Standard Deviation of Effective Radius	StaDev-F <sup>2</sup> , StaDev-C <sup>2</sup>
	Size Distribution	Vol-Con (0.05-15µm)

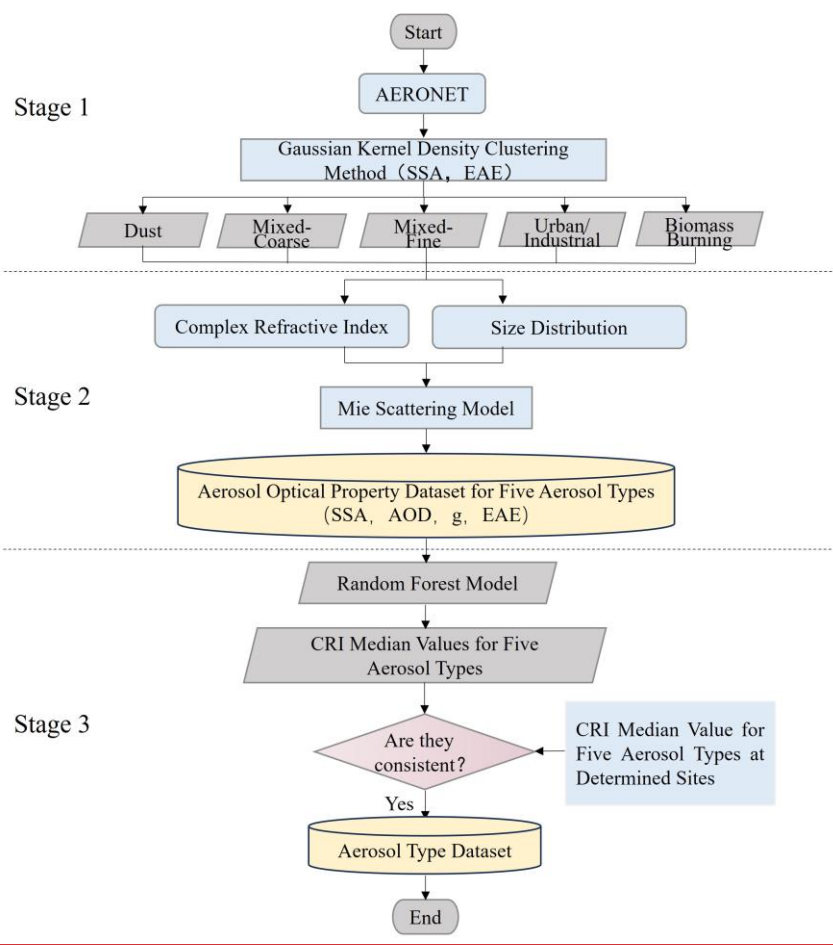
166 Note: <sup>1</sup> refers to wavelength in nm; <sup>2</sup> refers to different modes; EAE is Extinction Ångström Exponent; REFI is Imaginary Part of the  
 167 Complex Refractive Index; REFR is Real Part of the Complex Refractive Index; F refers to fine mode; C refers to coarse mode; EffRad is  
 168 Effective Radius; StaDev is standard deviation; Vol-Con is Volume concentration

### 169 3. Methods

170 A new aerosol classification typing hybrid approach that provides insight into  
171 spatiotemporal variations in aerosol pollution and climate impacts on a global scale is  
172 proposed in this study. In this approach, an aerosol optical properties database using  
173 the Mie scattering model was built for calculating rapidly unique aerosol-type features.  
174 Additionally, the approach introduced, for the first time, the median value of the  
175 complex refractive index (CRI) as the criterion for identifying the aerosol type. CRI, a  
176 key microphysical characteristic of aerosols, plays a significant role in determining  
177 their intrinsic optical properties, such as their ability to scatter and absorb light (Raut  
178 and Chazette, 2008). The CRI is also vital for determining aerosols' chemical and  
179 physical compositions (Dubovik and King, 2000) and the CRI value is known for pure  
180 aerosol components (Nandan et al., 2021). Unlike the mean, the median CRI value is  
181 employed in this research for it represents the central tendency of data, especially  
182 beneficial in skewed distributions or when outliers are present. This is particularly  
183 useful when an average value of a specific aerosol-type might be influenced by the  
184 presence of other aerosol types. Moreover, ~~Further,~~ we have selected the aerosol  
185 classification based on the source (as described in Section 1), according to the  
186 parameters applied in this study and the requirements for AOD retrieval. Figure 2  
187 shows the working flowchart of the new hybrid aerosol-type identification approach,  
188 including three stages: aerosol typing preliminary classification, aerosol optical  
189 database generation, and global aerosol typing identification and validation. The  
190 details of these three stages are as follows.







192

193

194 **Figure 2.** Flow chart of the new hybrid algorithm in aerosol type identification.

195 **3.1 Aerosol typing preliminary classification (Stage 1)**

196 Stage 1 aimed to solve the problem of obtaining a feature parameter dataset for  
 197 the baseline aerosol type. In previous studies, the Gaussian kernel density clustering  
 198 algorithm showed great potential for distinguishing the optical properties of different  
 199 aerosol types and determining their corresponding thresholds rapidly ( Kalapureddy et  
 200 al. 2009; Pathak et al. 2012). The high concentration value in each cluster generally  
 201 represents the dominant pattern of a specific aerosol type, particularly the data within  
 202 the window, taking the cluster centroid as the center and a specific distance as the  
 203 radius. Preliminary aerosol-type datasets can be generated by digging deep into the  
 204 distribution information of the effective radius, variance, and refractive index of the  
 205 data within the window. The spectral absorbability and particle size of aerosols guide  
 206 the identification of dust, carbonaceous, or hygroscopic aerosols; SSA indicates the

207 absorption of aerosol particles; and EAE describes aerosol particle size (Giles et al.,  
 208 2012). Consequently, in this study,  $SSA_{440nm}$  and  $EAE_{440-870nm}$  of 47 AERONET sites  
 209 and the Gaussian kernel density clustering~~Gaussian kernel density~~ method was used  
 210 to estimate the relative densities and determine the primary patterns of the dominant  
 211 aerosol types; here, the aerosol type was classified as a dust aerosol. Eqs. (1) and (2)  
 212 represent the kernel density and Gaussian kernel density clustering~~Gaussian kernel~~  
 213 ~~density~~ methods (Rosenblatt, 1956).

$$214 \quad f_{X(v)} = \frac{1}{L} \sum_{i=1}^L k_{\sigma} \left( \frac{\bar{x} - \bar{x}_i}{\sigma} \right), \quad (1)$$

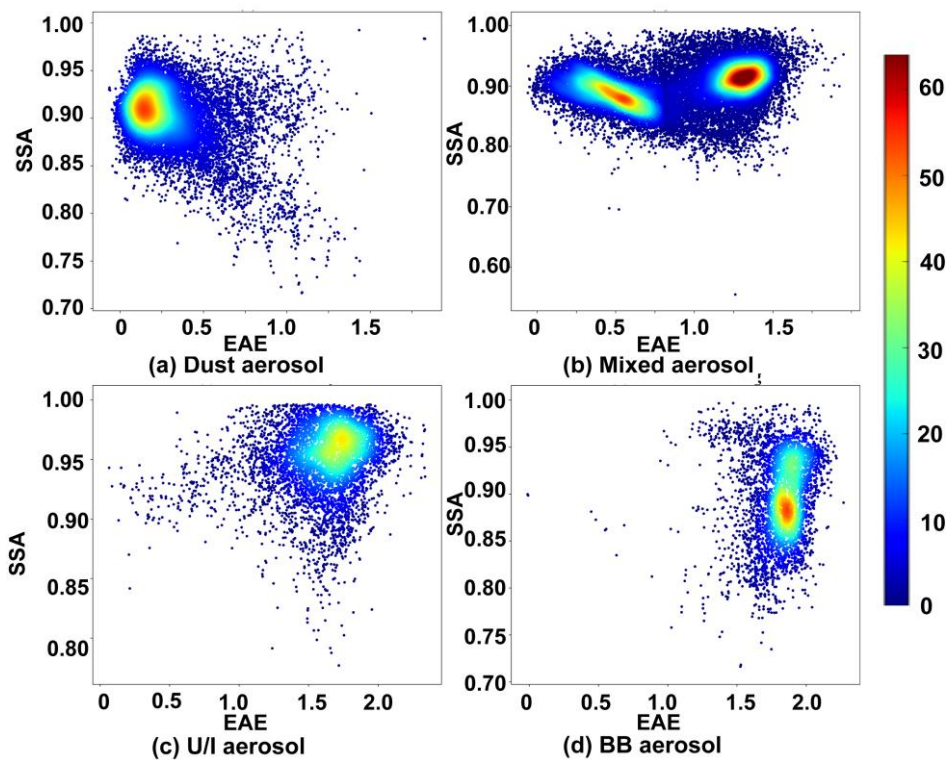
215 where  $f_{X(v)}$  denotes the kernel density and  $k_{\sigma}$  indicates the kernel function.  $x_1,$   
 216  $x_2 \dots x_L$  are the sample points of independent identical distribution. Mathematically,  
 217 kernel functions are symmetric, normalized, and sample-centric when used for density  
 218 estimation; this is best described by the Gaussian kernel equation given by Eq. (2).

$$219 \quad k_{\sigma} = \frac{1}{\sqrt{2\pi}\sigma} \exp\left(\frac{-|\bar{x} - \bar{x}_i|^2}{2\sigma^2}\right), \quad (2)$$

220 where  $\sigma$  is the kernel size used as a smoothing factor (Moraes et al., 2021).

221 The mixed aerosols comprised fine- and coarse-mode aerosols, indicated by  
 222  $EAE > 0.8$  and  $EAE \leq 0.8$ , respectively. Figure 3 shows the clustering distribution of  
 223 EAE and SSA using the Gaussian kernel density clustering~~Gaussian kernel density~~  
 224 method for different aerosol types at the 47 AERONET sites. For the dust aerosol  
 225 cluster, the density core area EAE was 0.1–0.3, and SSA was 0.89–0.94, implying that  
 226 it contained many coarse aerosol particles with moderate absorptivity. Furthermore,  
 227 the mixed aerosols had two distinct centers: one for the coarse-mode aerosols with a  
 228 median EAE value of 0.4, indicating that the cluster contained massive high-  
 229 absorption aerosols, and the other for fine-mode aerosols with a median EAE value of  
 230 1.3. Low-absorption aerosols were dominant in the cluster, similar to U/I aerosols.  
 231 Additionally, the density core region EAE of U/I aerosol was 1.5–1.8, and SSA was  
 232 0.94–0.97, implying the dominance of fine and low-absorption aerosols. Conversely,  
 233 BB aerosols had two indistinct centers. This is because, during biomass combustion,

234 gas and particulate matter emissions are limited by the combustion conditions, divided  
 235 into combustion and simmering. Combustion produces black smoke, and simmering  
 236 produces white smoke. Combustion, such as burning flames (grass) with high black  
 237 carbon content, has a strong absorption capacity, resulting in a low SSA. Simmering,  
 238 such as burning wood (i.e., trees), tends to be smoldering, lasts longer, has a weaker  
 239 absorption capacity, and has a higher SSA value. Therefore, despite possessing  
 240 different absorption characteristics, BB aerosols are defined as one aerosol type with  
 241 an unseparated center of combustion and simmering.



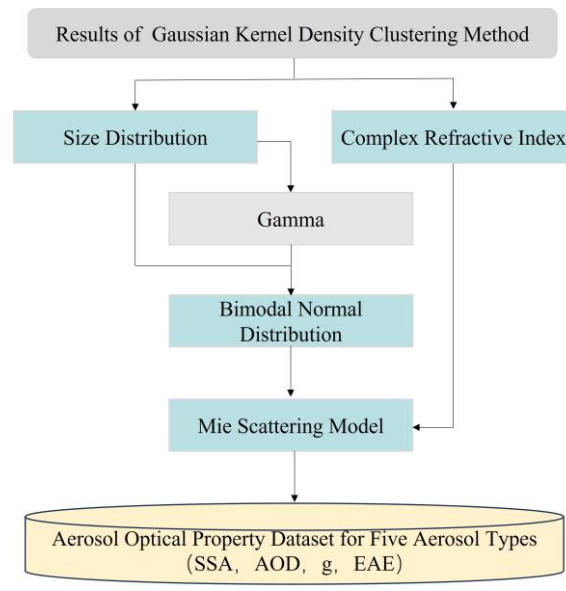
242

243 **Figure 3.** The clustering distribution of EAE and SSA using the [Gaussian kernel density clustering](#)  
 244 method for different aerosol types.

### 245 3.2 Aerosol optical database generation (Stage 2)

246 In stage 2, the aerosol optical parameter database was built using the aerosol size  
 247 distribution parameters, CRI, and Mie scattering model. The main reasons for  
 248 constructing an aerosol optical parameter database instead of using the AERONET  
 249 data directly are as follows: 1) many data are missed in AERONET, particularly those  
 250 for sites dominated by biomass combustion, which does not meet the requirements of  
 251 machine learning methods or traditional aerosol type identification algorithms; 2)

252 Calculating the optical properties of aerosols based on a fixed refractive index can  
 253 accurately determine aerosol types. Therefore, once the aerosol spectral distribution  
 254 parameters, such as effective radius, variance, and refractive index of the five aerosol  
 255 types, are determined in stage 1, the aerosol optical parameter database can be  
 256 constructed using the Mie scattering model in stage 2, assuming that aerosols are  
 257 spherical particles. The Mie scattering model is a simple, practical, and ideal spherical  
 258 particle model commonly used in radiation transport models (Michael et al., 1994).  
 259 Figure 4 shows the details involved in the building aerosol optical database. The  
 260 aerosol optical database has four major parameters (AOD, EAE, SSA, and g) at four  
 261 wavelengths (440, 675, 870, and 1020 nm, respectively).



262

263 **Figure 4.** The diagram of building aerosol optical property database.

264 ~~As shown in Figure 4, size distribution is a major parameter in building aerosol~~  
 265 ~~optical databases. Table 3 presents the aerosol size distribution parameters, including~~  
 266 ~~the effective radius and standard deviation range for the five aerosol types in the~~  
 267 ~~coarse and fine modes, which were calculated using the data in the window~~  
 268 ~~determined by the Gaussian kernel density algorithm. These aerosol size distribution~~  
 269 ~~parameters were used to build the aerosol optical database for the Mie scattering~~  
 270 ~~model.~~

271 **Table 3.** Size distribution parameters of five aerosol types in coarse and fine mode (unit:  $\mu\text{m}$ )

Aerosol type	REFF-fine	REFF-coarse	Std-fine	Std-coarse
Dust	0.05-0.42	1.3-2.65	0.5-0.8	0.4-0.7
Mixed-coarse	0.05-0.25	1.25-3.5	0.4-0.8	0.4-0.7
Mixed-fine	0.05-0.27	1.2-4.5	0.3-0.6	0.5-0.8
U/I	0.05-0.26	1.45-3.5	0.3-0.6	0.5-0.8
BB	0.05-0.17	1.35-4.5	0.3-0.5	0.5-0.8

272 Table 3 presents the aerosol size distribution parameters, including the effective  
273 radius and standard deviation range for the five aerosol types in coarse and fine modes,  
274 which were derived from the data window set by the Gaussian kernel density  
275 clustering algorithm. These aerosol size distribution parameters and the median CRI  
276 value were utilized to construct the optical database for the Mie scattering model.  
277 Many studies proven it is a reliable model with the advantage of lower computing  
278 load and high calculation accuracy (Zhao et al., 2008; Fu et al., 2009; Quirantes et al.,  
279 2019; Nandan et al., 2021).

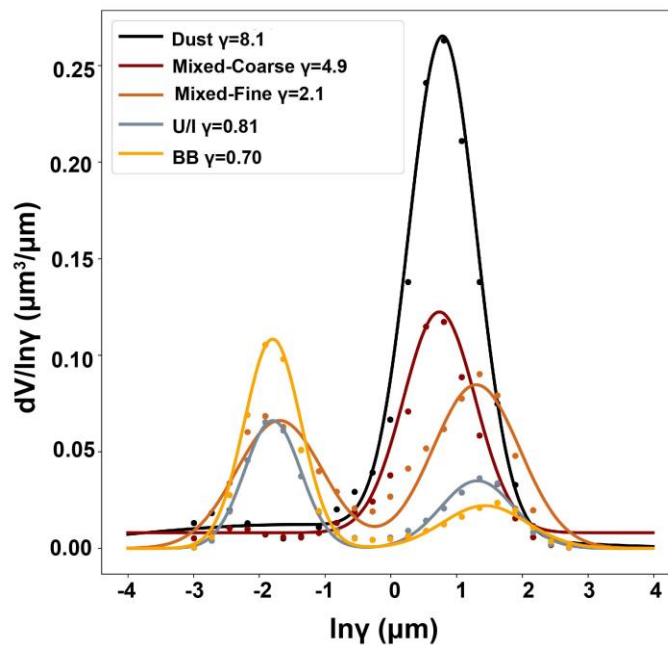
280 The Mie scattering model has various size distribution functions, including log-  
281 normal, power-law, and bimodal log-normal distributions, which describe the aerosol  
282 type. According to the particle radii provided by AERONET, the size distributions of  
283 different aerosol types can be divided into coarse and fine modes. The bimodal log-  
284 normal function [Eq. (3)] is reportedly the most suitable size distribution function for  
285 modeling aerosol particle size distribution (Remer et al., 2009):

$$286 \quad n(r) = \text{constant} \times r^{-4} \left\{ \exp\left(-\frac{(\ln r - \ln r_{g1})^2}{2 \ln^2 \sigma_{g1}}\right) + \gamma \exp\left(-\frac{(\ln r - \ln r_{g2})^2}{2 \ln^2 \sigma_{g2}}\right) \right\}, \quad (3)$$

287 where  $n(r)$  is the number of particles at different radii; constant is obtained by fitting;  
288 While  $r_{g1}$  and  $r_{g2}$  denote the radii,  $\sigma_{g1}$  and  $\sigma_{g2}$  denote the variances of the aerosol in the  
289 coarse and fine modes, respectively; and  $\gamma$  is determined by the volume distribution.  
290 In the bimodal normal distribution model,  $\gamma$  is the ratio of coarse to fine modes, which  
291 can be fitted by the volume distribution from AERONET; notably, volume distribution  
292 is the average of the standard aerosols obtained after clustering at the training sites.

293 Figure 5 shows the volume distributions of the different aerosol types. The

294 aerosol volume distribution of dust aerosol-dominant sites focuses on the large radius;  
 295 the peak value of  $\gamma$  was 8.1, and the radius of dust aerosols was 1.5–2.0  $\mu\text{m}$ .  
 296 Additionally, the mixed-coarse aerosol with the radius in the range of 0.04–0.2  $\mu\text{m}$   
 297 and 4.9 as the maximum value of  $\gamma$ . The mixed-fine aerosol had two obvious peaks:  
 298 one with a large radius, namely the coarse mode, with a radius of 2.2–3  $\mu\text{m}$  and 2.1 as  
 299 the peak point of  $\gamma$ ; a second with a small radius of 0.1–0.22  $\mu\text{m}$  and 0.14 as the peak  
 300 point of  $\gamma$ . Moreover, the volume distributions of U/I and BB aerosols were similar.  
 301 Both had a relatively low range of  $\gamma$  values at large radii and relatively high values at  
 302 small radii, with peak values of 0.81 and 0.7 for U/I and BB aerosols, respectively.



303

304 **Figure 5.** Volume distribution of the five aerosol types.

305 ~~The CRI of aerosols is another key parameter among aerosol optical properties; it~~  
 306 ~~determines inherent optical properties of aerosols, such as scattering and absorption~~  
 307 ~~(Raut and Chazette, 2008). The CRI is vital for determining aerosols' chemical and~~  
 308 ~~physical compositions (Dubovik and King, 2000). Aerosols in the real atmosphere are~~  
 309 ~~usually mixed with different types of particles, which a single refractive index cannot~~  
 310 ~~identify; however, the CRI represents the entire aerosol model in the atmosphere~~  
 311 ~~(Redemann et al., 2000). Ideally, the CRI and aerosol components can be mutually~~  
 312 ~~determined (Wu et al., 2021). Table 4 depicts the CRI standard values for the five~~

313 ~~aerosol types obtained by calculating the median value of the CRI of the dominant~~  
314 ~~aerosol type after Gaussian density clustering. These values were used as a baseline~~  
315 ~~for identifying the aerosol types in subsequent studies. As presented in Table 4, the~~  
316 ~~minimum imaginary index part is represented by the dust aerosol with CRI of~~  
317 ~~0.003396, 0.000731, 0.000639, and 0.000597 at 440, 675, 870, and 1020 nm,~~  
318 ~~respectively, owing to the weakest absorption of dust aerosols. Moreover, the~~  
319 ~~imaginary index part of the mixed fine aerosols (0.01) was close to that of the BB~~  
320 ~~aerosols (0.02) because of their similar absorption properties.~~

321 **Table 4.** Real and imaginary index of CRI for the five aerosol types (Bands:440/675/870/1020  
322 nm).

Aerosol Type	Imaginary Index	Real Index
Dust	0.003396/0.000731/0.000639/0.000597	1.4584/1.4681/1.4513/1.4376
Mixed-coarse	0.005766/0.002921/0.002383/0.002043	1.4291/1.4787/1.4745/1.4695
Mixed-fine	0.01075/0.008444/0.009147/0.008955	1.5001/1.5044/1.5056/1.4977
U/I	0.004315/0.004331/0.004419/0.004432	1.4372/1.4280/1.4264/1.4214
BB	0.01828/0.017862/0.018125/0.017858	1.5051/1.5190/1.5228/1.5185

323 The CRI is an inherent optical property of aerosols. Aerosols in the real  
324 atmosphere are usually mixed with different types of particles, which a single  
325 refractive index cannot identify; however, the CRI represents the entire aerosol model  
326 in the atmosphere (Redemann et al., 2000). Ideally, the CRI and aerosol components  
327 can be mutually determined (Wu et al., 2021). The CRI can effectively characterize  
328 the main properties of the aerosols and accurately quantify the difference between  
329 aerosol-type identification algorithms. Table 4 depicts the CRI standard values for the  
330 five aerosol types obtained by calculating the median value of the CRI of the  
331 dominant aerosol type after Gaussian kernel density clustering. These values were  
332 used as a baseline for identifying the aerosol types in subsequent studies. As presented  
333 in Table 4, the minimum imaginary index part is represented by the dust aerosol with  
334 CRI of 0.003396, 0.000731, 0.000639, and 0.000597 at 440, 675, 870, and 1020 nm,  
335 respectively, owing to the weakest absorption of dust aerosols. Moreover, the  
336 imaginary index part of the mixed-fine aerosols (0.01) was close to that of the BB



337 aerosols (0.02) because of their similar absorption properties.

338 Lastly, by fixing the CRI, changing the size distribution, and using the Mie  
339 scattering model, we generated the aerosol optical property database for five aerosols,  
340 including the data for AOD, EAE, SSA, and g. In the aerosol optical property  
341 database, AOD is the value obtained after eliminating the influence of the aerosol  
342 concentration. The AOD was obtained from the extinction cross section ( $C_{ext}$ )  
343 calculated using the Mie scattering model in Eqs. (3) and (4), where  $\beta_{ext}$  is the  
344 extinction coefficient,  $n(r)$  is the aerosol spectral distribution, and  $N(z)$  is the variation  
345 of aerosol concentration with height. Notably, the effect of aerosol concentration  
346 needs to be removed from the AOD when referring to aerosol optical properties. The  
347 AOD was normalized by dividing the aerosol optical thickness at the four  
348 wavelengths by the optical thickness at 440 nm. The other parameters (EAE, SSA,  
349 and g) were calculated using Eqs. (6) – (8).

$$350 \quad \beta_{e/s} = \int_{\gamma_{min}}^{\gamma_{max}} C_{ext/sca} n(r) dr , \quad (4)$$

$$351 \quad \tau_{e/s} = \int_0^{Z_{top}} \beta_{ext/sca} N(z) dz, \quad (5)$$

$$352 \quad EAE_{440-870nm} = - \frac{\ln(\tau_{440nm}) - \ln(\tau_{870nm})}{\ln(440) - \ln(870)} , \quad (6)$$

$$353 \quad SSA = \frac{\tau_s}{\tau_e} , \quad (7)$$

354 and

$$355 \quad g = \langle \cos\Theta \rangle = \frac{1}{2} \int_{-1}^1 p(\cos\Theta) \cos\Theta d \cos\Theta , \quad (8)$$

356 where  $\tau_{440}$  and  $\tau_{870}$  are the extinction optical depths of the aerosol at 440 and 870 nm,  
357 respectively,  $EAE_{440-870}$  nm is the extinction Ångström index from the 440 to 870 nm  
358 band, and  $\Theta$  denotes the scattering angle.

359 ~~The amount of data for the five aerosol types calculated using the Mie scattering~~  
360 ~~model is presented in Table 5. The least amount of data was observed for the mixed-~~

361 ~~fine aerosol owing to its small distribution range of effective variance. The largest~~  
 362 ~~data was observed for dust and mixed aerosols owing to their widely distributed~~  
 363 ~~effective radii. A total of 326400 datasets were present in the aerosol optical database,~~  
 364 ~~which meets the requirements for random forest algorithm.~~ ~~he amount of data for the~~  
 365 ~~five aerosol types calculated using the Mie scattering model is presented in Table 5.~~  
 366 ~~The least amount of data was observed for the mixed-fine aerosol owing to its small~~  
 367 ~~distribution range of effective variance. The largest data was observed for dust and~~  
 368 ~~mixed aerosols owing to their widely distributed effective radii. A total of 326400~~  
 369 ~~datasets were present in the aerosol optical database, which meets the requirements~~  
 370 ~~for random forest algorithm.~~

371 **Table 5.** The data size of optical database simulated by Mie scattering model.

<b>Total</b>	<b>Dust</b>	<b>Mixed-coarse</b>	<b>Mixed-fine</b>	<b>U/I</b>	<b>BB</b>
326400	88200	96000	42000	51840	48360

### 372 3.3 Global aerosol type identification and validation (Stage 3)

373 In stage 3, the random forest model was introduced to the aerosol-type  
 374 identification algorithm. The random forest model is an integrated model based on  
 375 classification and regression trees, in which multiple trees are aggregated using  
 376 majority voting and averaging for classification and regression (Breiman, 2001). The  
 377 model has a high prediction accuracy, excellent tolerance for abnormal values and  
 378 noise, and a hard overfit. In a comparison by Fernandez (2014), the random forest  
 379 algorithm ranked as the top performer among 179 classification algorithms. In  
 380 addition, the evaluation matrix was brought into this study, and it further  
 381 quantitatively assesses the performance of the Gaussian density clustering algorithm  
 382 and the new hybrid algorithm. The metric indexes include accuracy, recall, precision,  
 383 and F-scores (Reddy et al., 2022). Here, the indexes are adjusted to micro-precision,  
 384 micro-recall, micro-F1-score, and accuracy to solve the multi-classification problem.  
 385 Micro refers to the weighted average of the five aerosol types rather than the  
 386 arithmetic mean, due to the large difference in sample size among the five aerosol  
 387 types, the arithmetic mean is highly susceptible to the influence of very large or very

~~few sample size aerosol types. The random forest model is an integrated model based on classification and regression trees, in which multiple trees are aggregated using majority voting and averaging for classification and regression (Breiman, 2001). The model has a high prediction accuracy, excellent tolerance for abnormal values and noise, and a hard overfit. In a comparison by Fernandez (2014), the random forest algorithm performed the best among 179 classification algorithms. Moreover~~

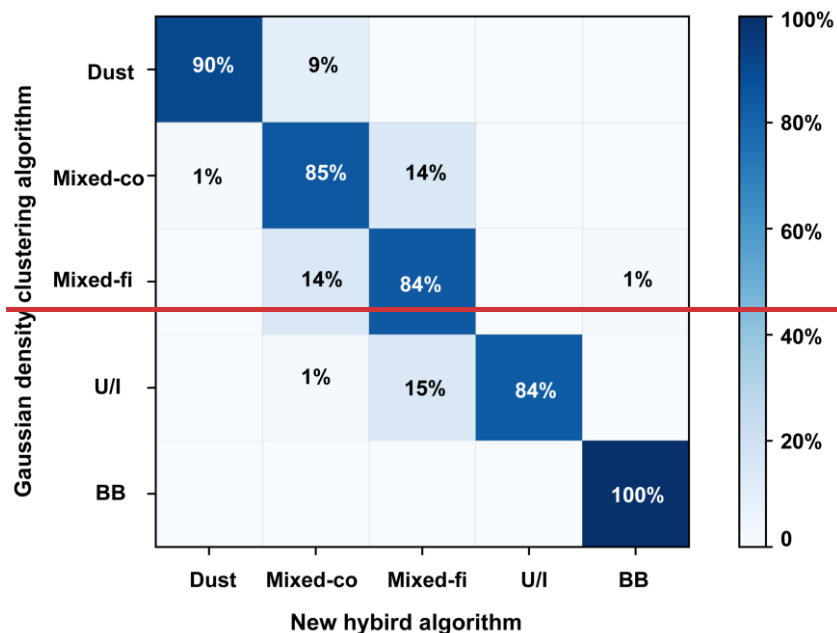
The input parameters for random forest model training, including SSA<sub>440nm</sub>, SSA<sub>675nm</sub>, SSA<sub>870nm</sub>, SSA<sub>1020nm</sub>, g<sub>440nm</sub>, g<sub>675nm</sub>, g<sub>870nm</sub>, g<sub>1020nm</sub>, normalized AOD<sub>440nm</sub>, AOD<sub>675nm</sub>, AOD<sub>870nm</sub>, AOD<sub>1020nm</sub>, and EAE<sub>440-870nm</sub>, were selected from the aerosol optical property database, and the expected output values were the specific aerosol types. The random forest model was optimized and the parameters were determined using the grid-searching method. The parameters, including n\_estimators (classifier), max\_features (maximum feature value), and min\_samples\_leaf (minimum number of samples for nodes), were set as 160, 10, 12, and 12, respectively. Then, based on the trained and optimized model, aerosol typing of any AERONET site in different regions of the world can be identified quickly. —Generating the aerosol type distribution map on a global scale is vital for regional and global climate studies and ground remote sensing.

## 4 Results

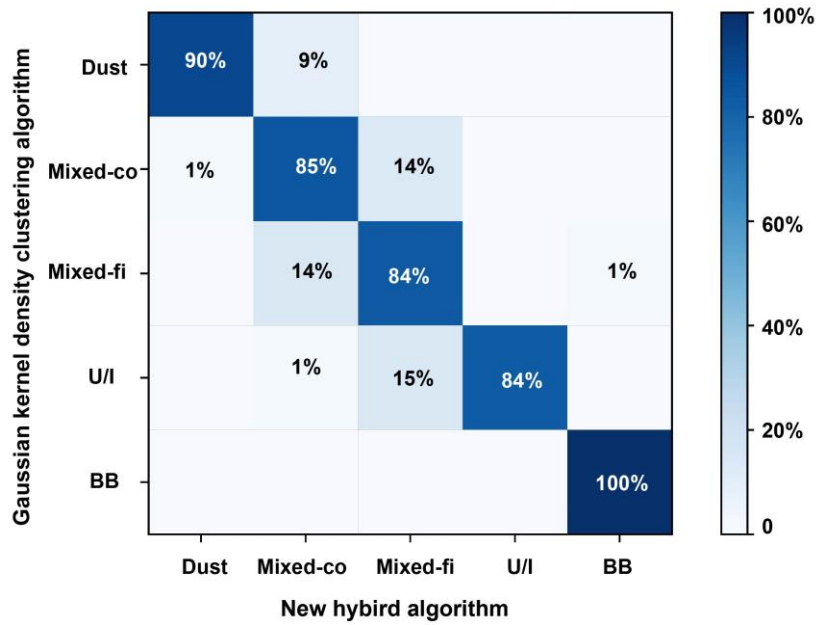
### 4.1 Algorithm comparison

To demonstrate the effectiveness of the new hybrid algorithm, its performance was compared with that of ~~Gaussian kernel density clustering~~~~Gaussian density clustering~~ algorithm. Figure 6 shows the confusion matrix between the new hybrid and Gaussian kernel density clustering algorithms in identifying aerosol types. The results of the new hybrid algorithm showed 90% consistency with that from the Gaussian kernel density clustering algorithm, in delineating dusty aerosols, indicating that its efficiency in identifying dust. For mixed-coarse aerosols, the consistency reached 85%, with 14% identified as mixed-fine aerosols, 1% as dust by the new

416 hybrid algorithm, and 15% as mixed-coarse aerosols by the Gaussian kernel density  
 417 clustering algorithm. Similarly, for mixed-fine aerosols, both algorithms showed 84%  
 418 consistency, with 14% identified as a mixed-coarse aerosol by ~~the~~ new -hybrid  
 419 algorithm and as a mixed-fine aerosol by the Gaussian kernel density cluster  
 420 algorithm. Furthermore, both algorithms identified 84% of U/I aerosols correctly, with  
 421 the remaining 16% identified as mixed aerosols (fine and coarse). Lastly, the  
 422 classification of BB aerosols using these two methods was the same. Overall, the  
 423 Gaussian kernel density clustering and new hybrid algorithms were consistent in dust,  
 424 mixed-coarse, U/I, and BB aerosol identification.



425



426

427 **Figure 6.** The confusion matrix between Gaussian kernel density clustering and new hybrid  
 428 algorithm.

429 Table 5 shows the metric index value of the random forest algorithm in the new  
 430 hybrid algorithm. The micro-precision, micro-recall, micro-F1 score, and accuracy are  
 431 0.95, 0.89, 0.91, and 0.89, respectively. These metrics are derived from the core  
 432 values of the window, as determined by the Gaussian density clustering algorithm.  
 433 Consequently, the strong performance of these indicators further confirms the efficacy  
 434 and reliability of the newly developed hybrid algorithm.

435 **Table 5.** Matrix evaluation between new hybrid classification algorithm and Gaussian kernel  
 436 density clustering algorithm

	<u>Micro-Precision</u>	<u>Micro-Recall</u>	<u>Micro-F1-Score</u>	<u>Accuracy</u>
<u>New Hybrid algorithm</u>	<u>0.95</u>	<u>0.89</u>	<u>0.91</u>	<u>0.89</u>

437 As described in the Methods section, a specific aerosol type theoretically has a  
 438 fixed CRI owing to its constant composition. The CRI characterizes the mixture  
 439 composition of aerosol particles and is a key parameter controlling the inherent  
 440 scattering and absorption characteristics of aerosol particles. To further analyze the  
 441 accuracy of the new algorithm, the aerosol CRI was applied as a key criterion for  
 442 aerosol identification. The CRI has two parts: imaginary and real. The imaginary part  
 443 indicates radiation absorption by aerosols, with a small value signifying a small

444 absorption. Because the radiation of aerosols is more dependent on the imaginary than  
445 the real part, the imaginary part is essential for inferring the optical properties and  
446 aerosol types. Hence, we compared the real and imaginary parts of the CRI calculated  
447 using the new hybrid and Gaussian kernel density clustering algorithms.

448 ~~As described in the Methods section, a specific aerosol type theoretically has a~~  
449 ~~fixed CRI owing to its constant composition. The CRI characterizes the mixture~~  
450 ~~composition of aerosol particles and is a key parameter controlling the inherent~~  
451 ~~scattering and absorption characteristics of aerosol particles. To further analyze the~~  
452 ~~accuracy of the new algorithm, the aerosol CRI was applied as a key criterion for~~  
453 ~~aerosol identification. The CRI has two parts: imaginary and real. The imaginary part~~  
454 ~~indicates radiation absorption by aerosols, with a small value signifying a small~~  
455 ~~absorption. Because the radiation of aerosols is more dependent on the imaginary than~~  
456 ~~the real part, the imaginary part is essential for inferring the optical properties and~~  
457 ~~aerosol types. Hence, we compared the real and imaginary parts of the CRI calculated~~  
458 ~~using the hybrid and Gaussian density clustering algorithms.~~

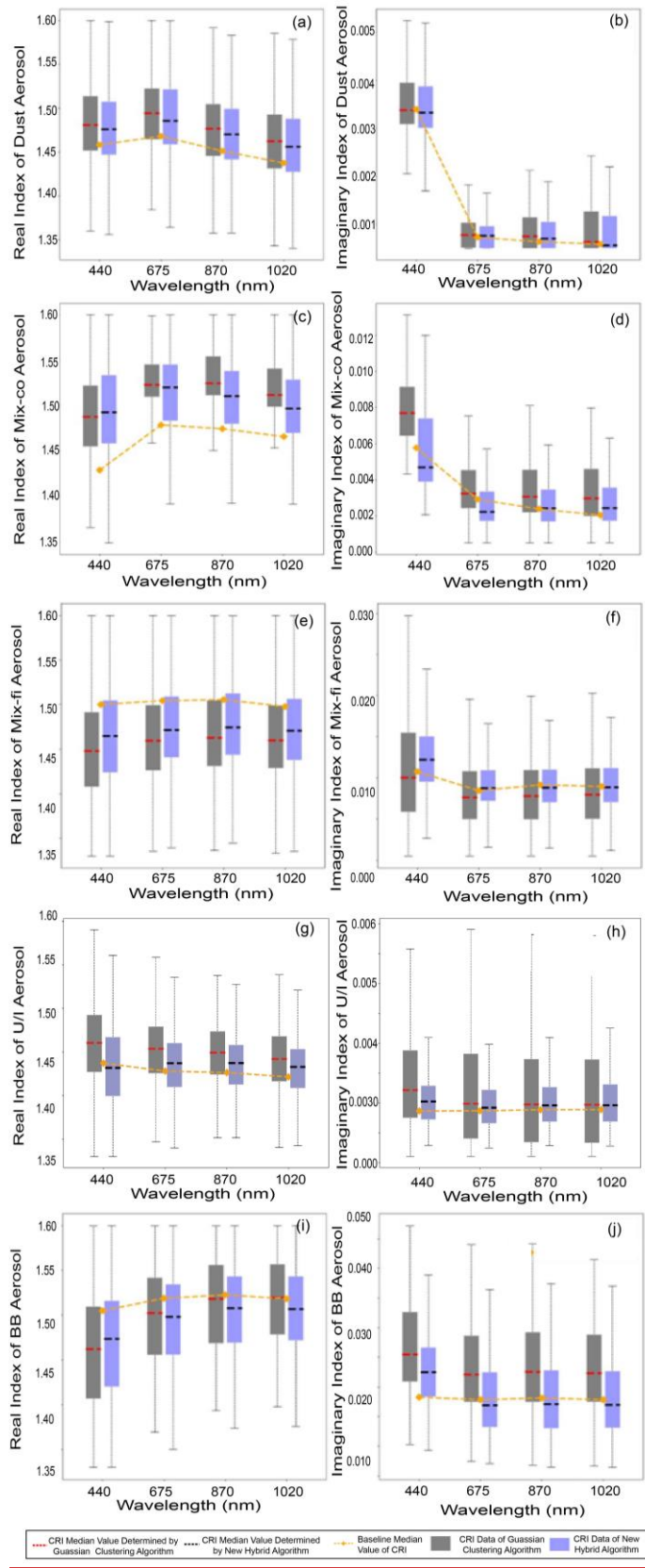
459 Figure 7 shows box plots of the aerosol CRI for dust, mixed-coarse, mixed-fine,  
460 U/I, and BB aerosols using the new hybrid classification and Gaussian kernel density  
461 clustering algorithms. Based on the principle that the CRI of aerosols is fixed under  
462 ideal conditions, the closer the median value of the CRI of the identified aerosol type  
463 is to the median value of the benchmark CRI, the more accurate is the identification  
464 method.

465 As shown in Figures 7 (a) and (f), the median values of the CRI real part for dust  
466 aerosol are in the range 1.45–1.53 at four bands, and those of the imaginary part are  
467 0.003–0.004 at 440 nm; further, the values in other bands decrease rapidly as  
468 wavelength increases. The imaginary part of CRI represents the absorption of light by  
469 the aerosol, with a small absorption indicating strong scattering. The results of the  
470 imaginary part are consistent with the spectral dependence properties of dust-based  
471 aerosols according to the wavelength. This is primarily because dust aerosols,  
472 composed of clay, quartz, and hematite, exhibit strong absorption in the blue band  
473 (440 nm) and low absorption in the visible and near-infrared bands. For the dust

474 aerosols, the CRI determined by the two methods did not differ much. However, the  
475 median value of the CRI obtained using the new hybrid algorithm was slightly closer  
476 to the benchmark CRI than that obtained using the Gaussian kernel density clustering  
477 algorithm for dust aerosols. Therefore, the new hybrid algorithm was concluded to be  
478 more accurate in identifying dust aerosol.

479 Figures 7 (b) and (g) show the median values of the CRI real part for mixed-  
480 coarse aerosol is 1.47–1.55 at four bands using the new hybrid algorithm, but the  
481 imaginary part is 0.004–0.009 at 440 nm. However, the real part is 1.44–1.50 at four  
482 bands determined by Gaussian kernel density clustering algorithm, and the imaginary  
483 part is 0.006–0.009 at 440nm. The median value of the hybrid algorithm was closer to  
484 the baseline median value than that of the Gaussian kernel density clustering  
485 algorithm for both the real and imaginary parts.

486 Figures 7 (c) and (h) show the median value of the CRI real part for mixed-fine  
487 aerosols determined using the new hybrid and Gaussian kernel density clustering  
488 algorithms, which was 1.42–1.51 at four bands. This result is close to the range (1.44–  
489 1.52) reported by Wu (2021) in Beijing using a random forest algorithm. The median  
490 CRI of the real part at four bands and imaginary part at the (675–870–1020 nm) bands  
491 were close to the baseline median value for the new algorithm. Additionally, the  
492 median value of the imaginary part was lower than that of the new hybrid algorithm  
493 and further from baseline data for the identifying aerosol type results mixed with 14%  
494 coarse aerosols. Mixed coarse aerosols result in weaker absorption. Hence, the new



495

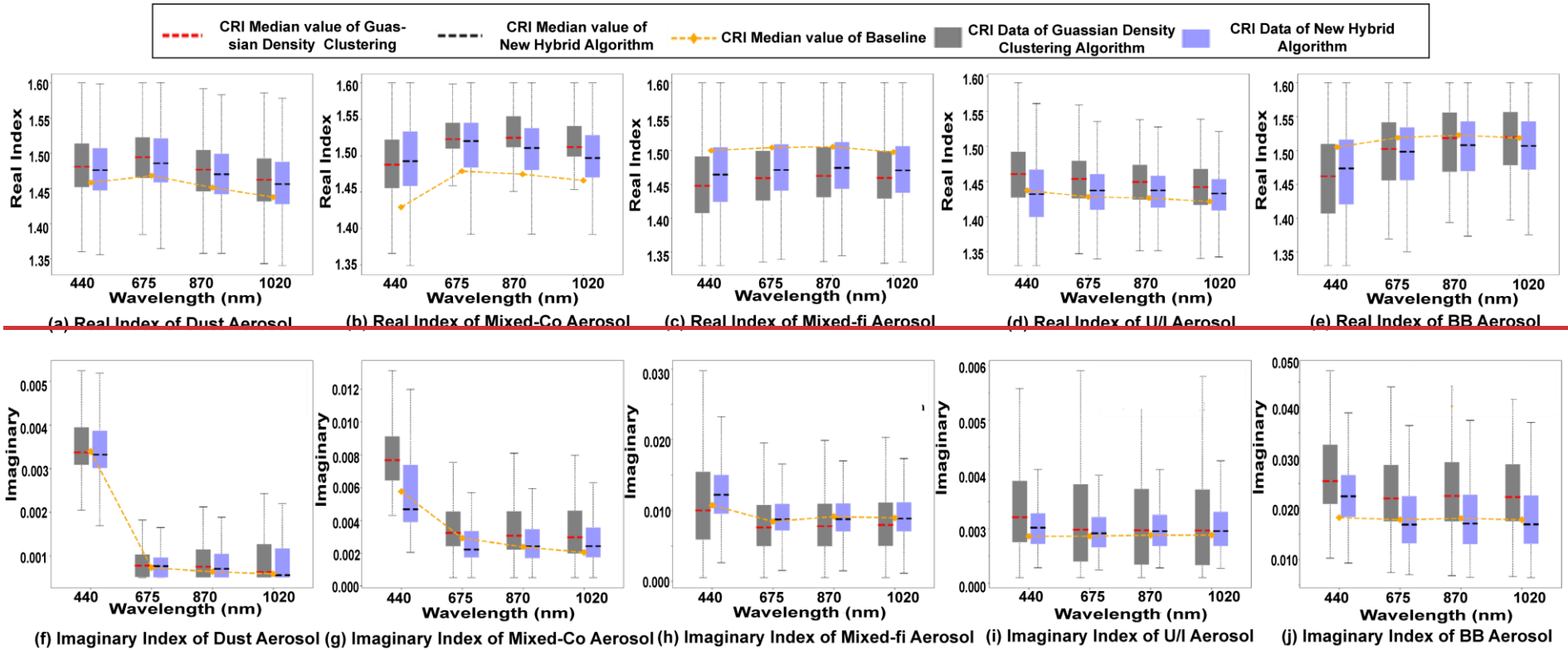
496

497

498

**Figure 7.** Box plots of the real index (left) and the imaginary (right) index of the CRI for (a-b) dust, (c-d) mixed-coarse, (e-f) mixed-fine aerosol, (g-h) U/I, and (i-j) BB aerosol identified by the Gaussian kernel density clustering algorithm and new hybrid algorithm, respectively.





500 **Figure 7.** Box plots of the real index and the imaginary index of the CRI for (a) dust, (b) mixed coarse, (c) mixed fine aerosol, (d)U/I, and (e) BB aerosol identified  
 501 by the Gaussian density clustering algorithm and new hybrid algorithm, respectively (the upper line is the real part, and the bottom line is the imaginary part).  
 502

503 hybrid algorithm performed better at identifying mixed-fine aerosols than the  
504 Gaussian kernel density clustering algorithm.

505 Similarly, as seen in Figures 7 (d) and (i), the median value of the CRI real part  
506 for U/I aerosol identified using the new hybrid algorithm was 1.39–1.47. This median  
507 value was lower than that of the mixed-fine aerosols. This is because the real part  
508 indicates the absorption ability of aerosols, and the absorption ability of U/I aerosols  
509 was less than that of mixed-fine aerosols. For the imaginary part also, the new hybrid  
510 algorithm performed slightly better than the Gaussian kernel density clustering  
511 algorithm at the four bands.

512 For BB aerosols, the median value of the real part generated using the new hybrid  
513 algorithm differed slightly from that generated by the Gaussian kernel density  
514 clustering algorithm. Additionally, the median obtained using the Gaussian kernel  
515 density clustering algorithm was closer to the baseline. Furthermore, when analyzing  
516 the imaginary part, the new hybrid algorithm performed much better than the  
517 Gaussian kernel density clustering algorithm. Even with a 100% concordance rate  
518 between the new hybrid and Gaussian kernel density clustering algorithms in  
519 identifying BB aerosols, the refractive index still differed. This result indicates that 1%  
520 of mixed-fine aerosols classified using the Gaussian kernel density clustering  
521 algorithm were correctly identified as BB aerosols by the new algorithm. Overall,  
522 these results demonstrate that the new algorithm is reliable.

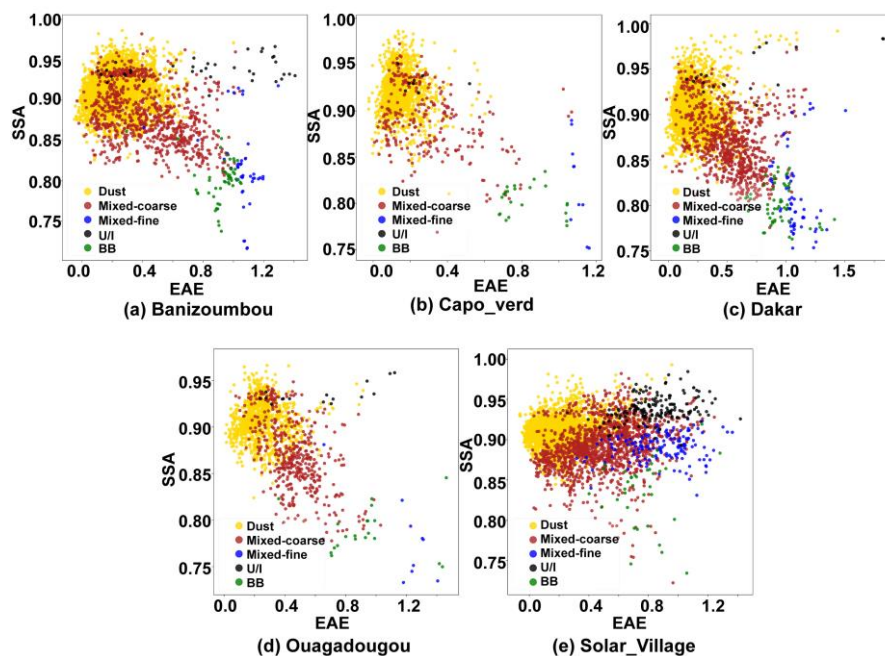
523 Additionally, in this study, the number of 326400 data points from optical  
524 parameters database and 98000 observed data for calculation spans from Jan.1st,1993  
525 to Dec.31st,2021, passing through Gaussian kernel density clustering algorithm and  
526 new hybrid algorithm Python progresses, which is archived on the personal Windows  
527 system computer (Intel® Core™ i7-10710U,16G DDR4 2666MHz, 512G PCIE SSD).  
528 The computational time for the two algorithms indicates the new hybrid algorithm  
529 runs faster than the Gaussian kernel density clustering algorithm with huge quantities

530 of data and trained in advance, which can obtain aerosol type in 20 seconds, in  
531 contrast, it will take 30 to 40 seconds to obtain aerosol type in one site by using the  
532 Gaussian algorithm.

## 533 4.2 Aerosol type determination for typical sites

### 534 4.2.1 Dust aerosol

535 Figure 8 shows the aerosol types obtained using the new hybrid algorithm for the  
536 five sites selected for dust aerosol identification. According to the prediction by the  
537 new hybrid algorithm, the aerosols at these five sites mainly contained dust aerosols  
538 along with a small amount of U/I, mixed-fine, and BB aerosols, and a large amount of  
539 mixed coarse aerosols. This shows that other types of aerosols invaded these areas  
540 besides dust aerosol. BB aerosols may have been transferred from the southern  
541 African savannah. Additionally, U/I aerosols could be from industrial cities, such as  
542 Dakar, Abidjan, and Lagos, which are dominated by anthropogenic aerosols and are  
543 close to the AERONET sites.



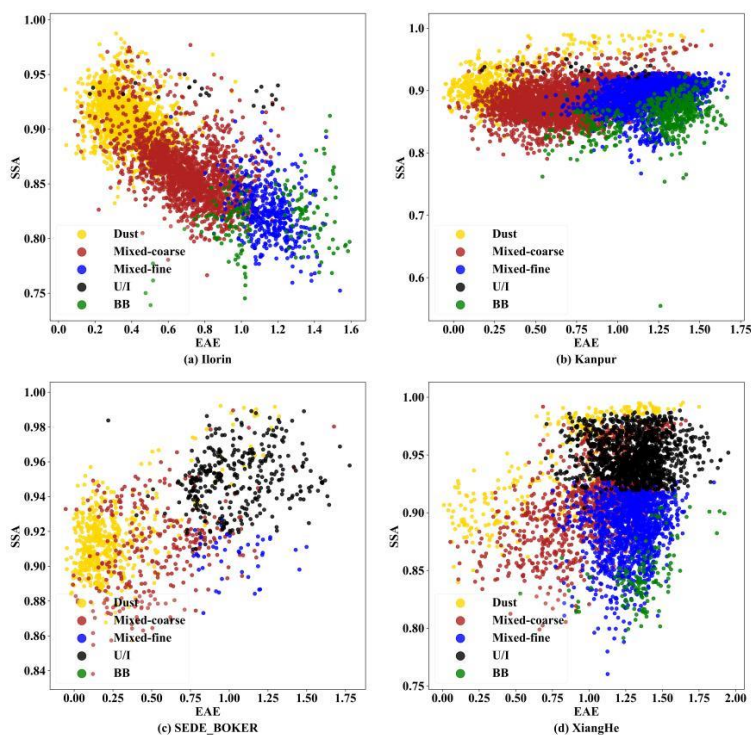
544  
545 **Figure 8.** Identification of dust aerosol at dominant aerosol sites.

### 546 4.2.2 Mixed aerosol

547 Besides Ilorin in Africa, the mixed aerosol AERONET sites, including Kanpur,

548 Sede\_Boker, and XiangHe, are in Asia. The aerosol types at these four sites were  
 549 determined using the new hybrid algorithm (Figure 9). Mixed coarse aerosols  
 550 dominated the Kanpur, Ilorin, and ~~Sede-Sede~~ Boker sites, and mixed fine aerosols  
 551 dominated XiangHe. Part of the dust in Xianghe could be due to the Takla Desert in  
 552 spring and the westerly winds prevailing in western China, which transported dust  
 553 aerosols over long distances. Additionally, the U/I aerosol in Xianghe could be a result  
 554 of human activities, construction emissions, and fuel burning in winter. The BB  
 555 aerosol was traced to the burning of a small amount of biomass in Xianghe, located in  
 556 a suburban area.

557 Furthermore, excluding dust aerosols, we observed BB and U/I aerosols in the  
 558 Kanpur site in the Ganges Basin of India. A certain amount of U/I and dust aerosols  
 559 were also observed in ~~Sede-Sede~~ Boker, located in the industrial center of Israel,  
 560 possibly from the Arabian desert. Lastly, Ilorin had the most dust and least BB  
 561 aerosols because it is located in central Africa, often affected by the Saharan Desert  
 562 and African savannah.

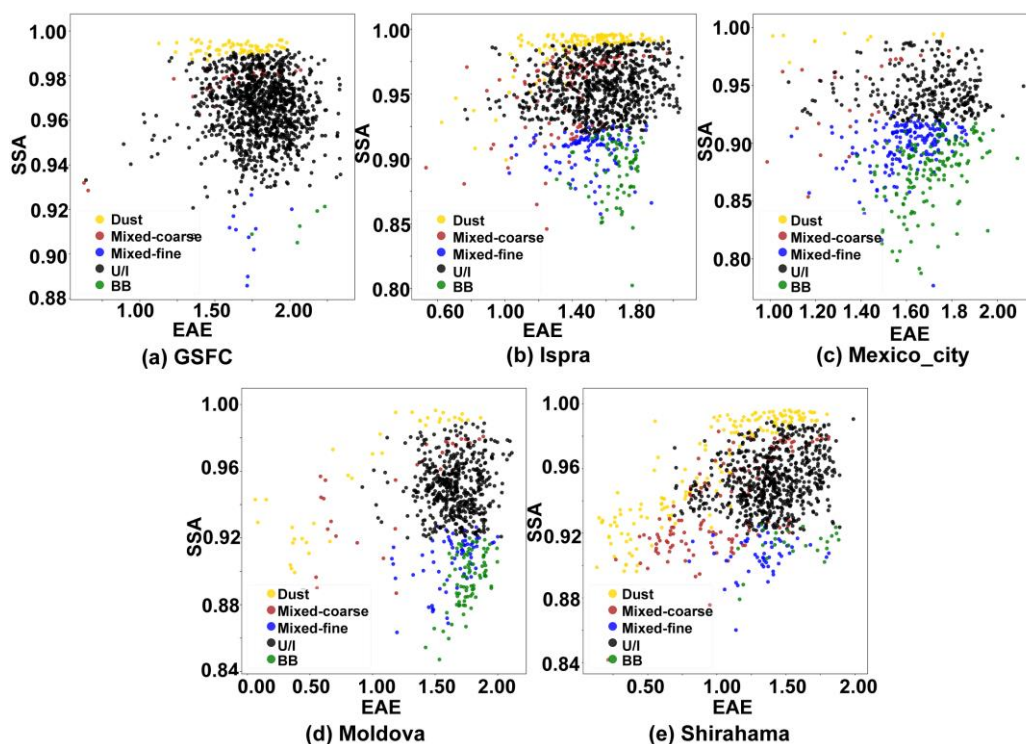


563  
 564 **Figure 9.** Same as Figure 8 but for Mixed aerosol.

### 565 **4.2.3 Urban/industrial aerosol**

566 All the selected AERONET sites for evaluating the performance of the new  
567 hybrid algorithm in terms of U/I aerosol identification are in Europe or North America  
568 (Figure 10). GSFC is located in the densely populated and industrially developed area  
569 of Washington in the United States, explaining its complex aerosol type dominated by  
570 the U/I aerosol followed by a few mixed and BB aerosols and a small amount of dust  
571 aerosols.

572 Ispra is in Turin, one of Italy's largest industrial centers. However, dust-type  
573 aerosols were identified, possibly transported from the Libyan desert when Italian  
574 winters were controlled by southwesterly winds. Moreover, Mexico, where the  
575 Mexico City site is located, is an industrialized country with modern industries and  
576 agriculture, abundant oil production, and a dense population. Nevertheless, we  
577 identified dust, mixed coarse, and BB aerosols in this site using the new hybrid  
578 algorithm. These aerosol types could be from the Chihuahuan Desert, an inland desert  
579 covering 12% of Mexico's area and a major source of coarse and dust aerosols.  
580 Additionally, the literature shows that Mexico City is surrounded by forested  
581 mountains, which experience many wildfires during the dry period between  
582 November and May; this accounts for BB aerosols in Mexico City (Yokelson et al.  
583 2007). Finally, the BB aerosols identified at the Moldova site could be attributed to its  
584 rich vegetation cover.

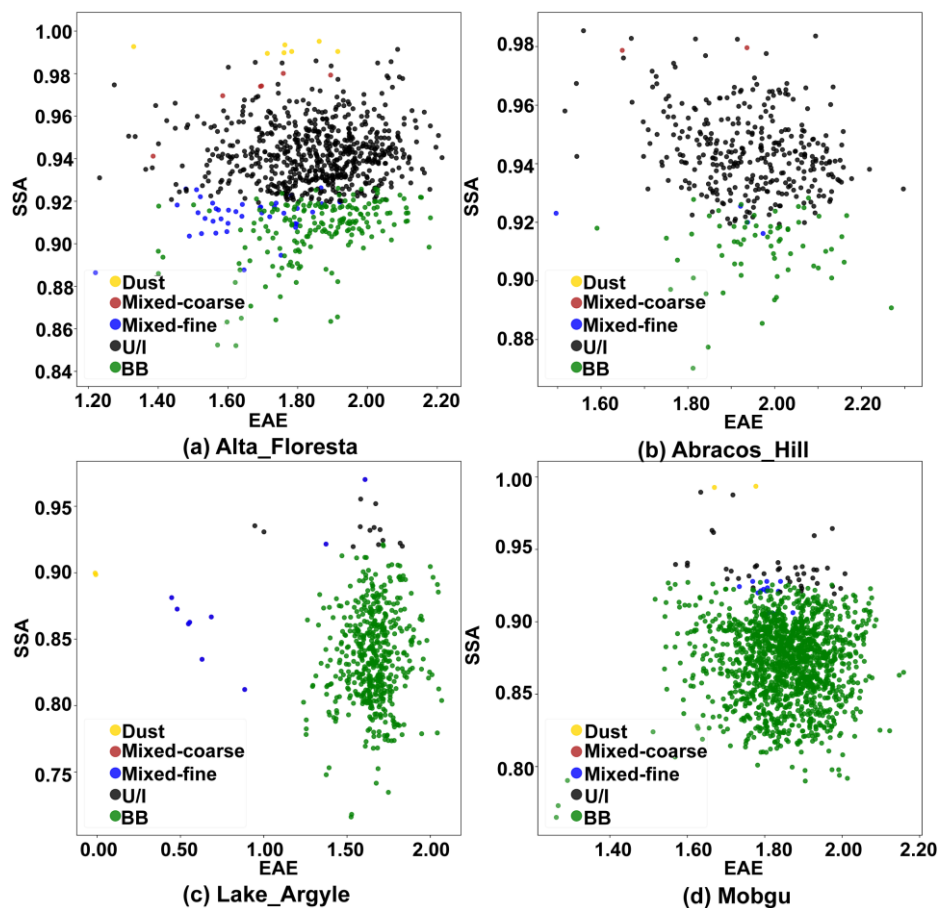


585  
586

**Figure 10.** Same as Figure 9 but for urban/industrial aerosol.

587 **4.2.4 Biomass burning aerosol**

588 The selected sites were mainly located in the mountains and highlands. Figure 11  
 589 shows the aerosol types identified using the new hybrid algorithm. Large amounts of  
 590 BB aerosols were identified at all sites. Additionally, a small amount of dust and  
 591 mixed-coarse aerosols were identified at the Alta-Alta Floresta site, transported over  
 592 a long distance from the Patagonian Desert in Argentina, in southern South America.  
 593 Moreover, the city where the site is located is industrially developed and has a large  
 594 population; therefore, more U/I aerosols were identified using the new hybrid  
 595 algorithm. The geographically close Abracos\_Hill and Alta-Alta Floresta sites were  
 596 characterized by the same aerosol type and source. Furthermore, one data point in  
 597 Lake Argyle was classified as a dust aerosol. This means that, although the site is  
 598 located on the Kimberley Plateau, Australia has a large desert area, and coarse  
 599 aerosols still exist. Lastly, a few U/I and several dust-type aerosols were identified at  
 600 the Mongu site, possibly caused by aerosol emissions from nearby cities and dust  
 601 transport from the Saharan Desert.



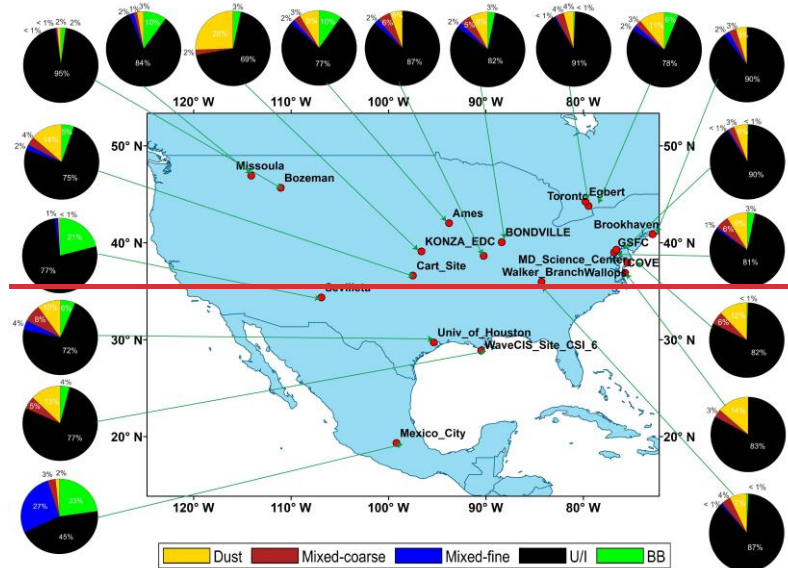
602  
603 **Figure 11.** Same as Figure 10 but for BB aerosol.

604 **4.3 Aerosol type distribution on a global scale**

605 Given the advantages and accuracy of the new hybrid algorithm in identifying  
 606 aerosol types, we used it to divide the data of AERONET sites in different regions of  
 607 the world to obtain global aerosol type distribution information. The aerosol types of  
 608 each continent are shown in Figures 12-16. Additionally, Figure 17 shows the global  
 609 aerosol-type distribution. Notably, the pie chart was placed on each site in the study,  
 610 which is a "point source" assessment of the aerosol type and does not represent the  
 611 entire region (the size of the pie chart is independent of the optical properties).  
 612 Moreover, the sites were screened, and only those with valid data of > 100 aerosol  
 613 types were considered; however, offshore sites and sites classified as marine aerosol-  
 614 dominated by other literature were excluded.

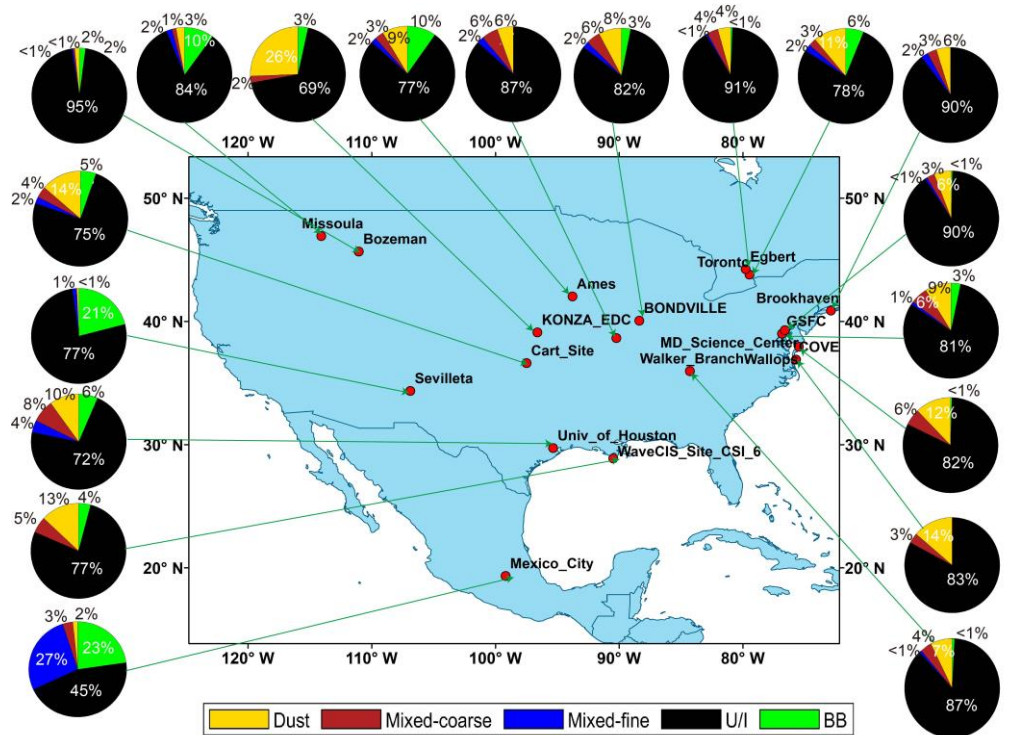
615 Figure 12 shows pie charts of the aerosol types for each scanned AERONET site  
 616 in North America. The U/I aerosols, particularly in most mid-eastern regions,

617 contained mixed and small amounts of biomass aerosols. Additionally, the AERONET  
 618 sites in large cities, such as Chicago, New York, Toronto, Ottawa, and Boston, had U/I  
 619 aerosols. Many studies have shown that dust aerosols from the Saharan Desert can  
 620 cross the Atlantic Ocean to North America in summer. Moreover, there is an inland  
 621 desert in western North America, the Chihuahua Desert, responsible for a small  
 622 amount of dust and mixed aerosols at the AERONET sites in North America.  
 623 Additionally, wildfires in western North America and household wood burning  
 624 contribute to most BB aerosols yearly. The central region site is affected by the  
 625 environment, with an increased proportion of BB aerosols, and U/I aerosols are still  
 626 prevalent because the site is located in a large city and is densely populated.



627

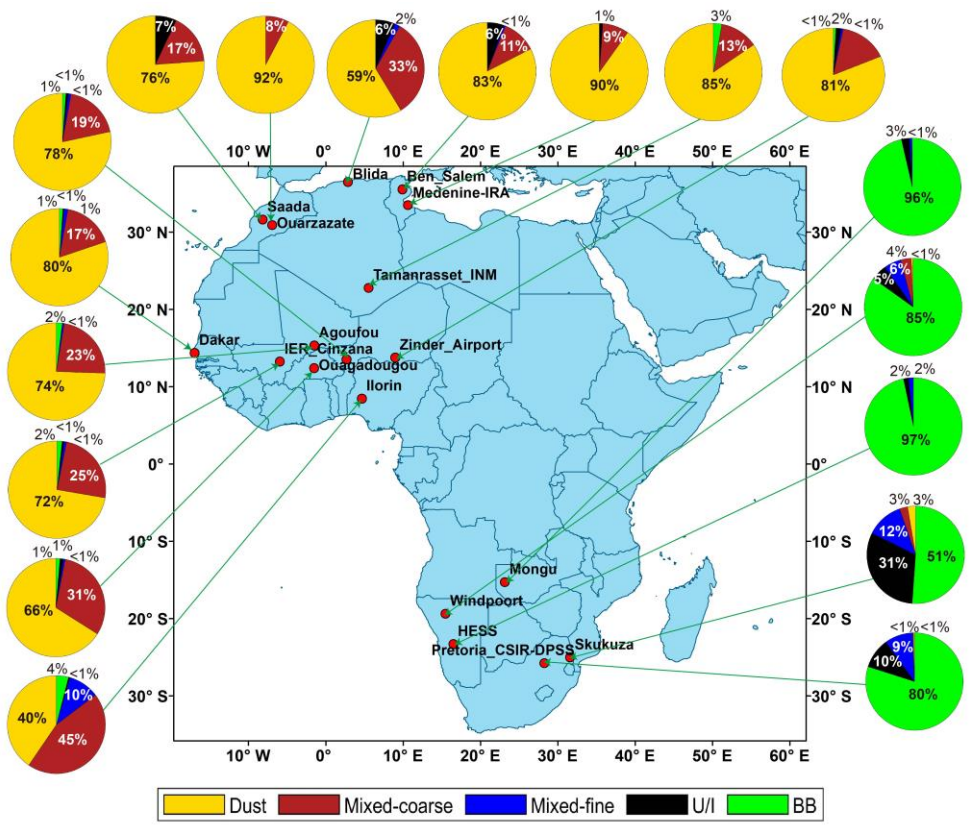
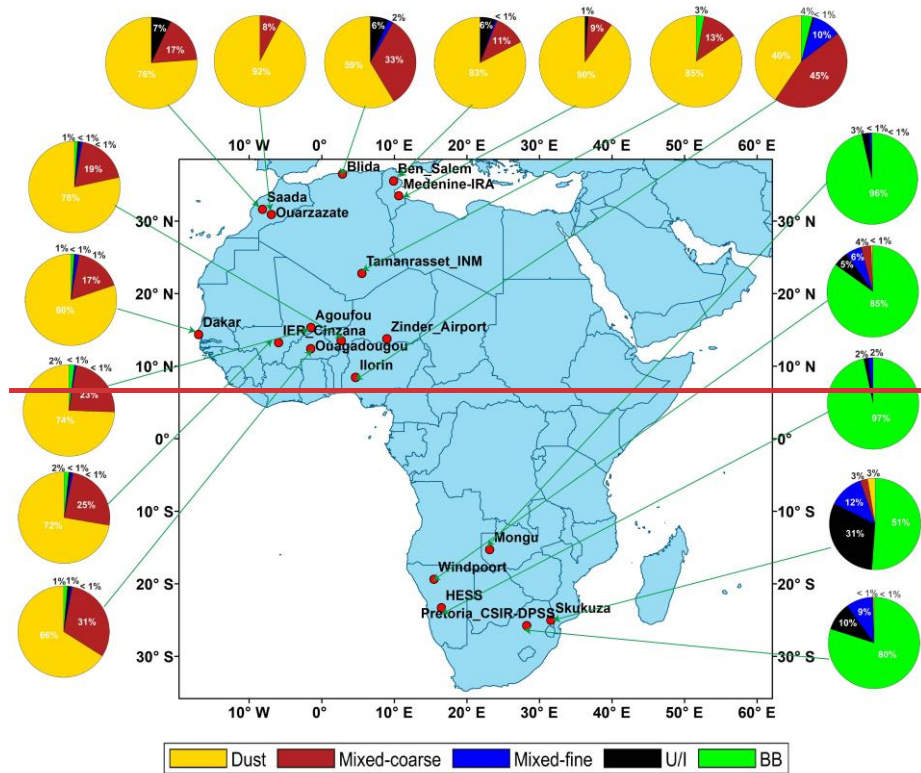




628

629 **Figure 12.** Pie charts of the aerosol types at the major sites of North American.

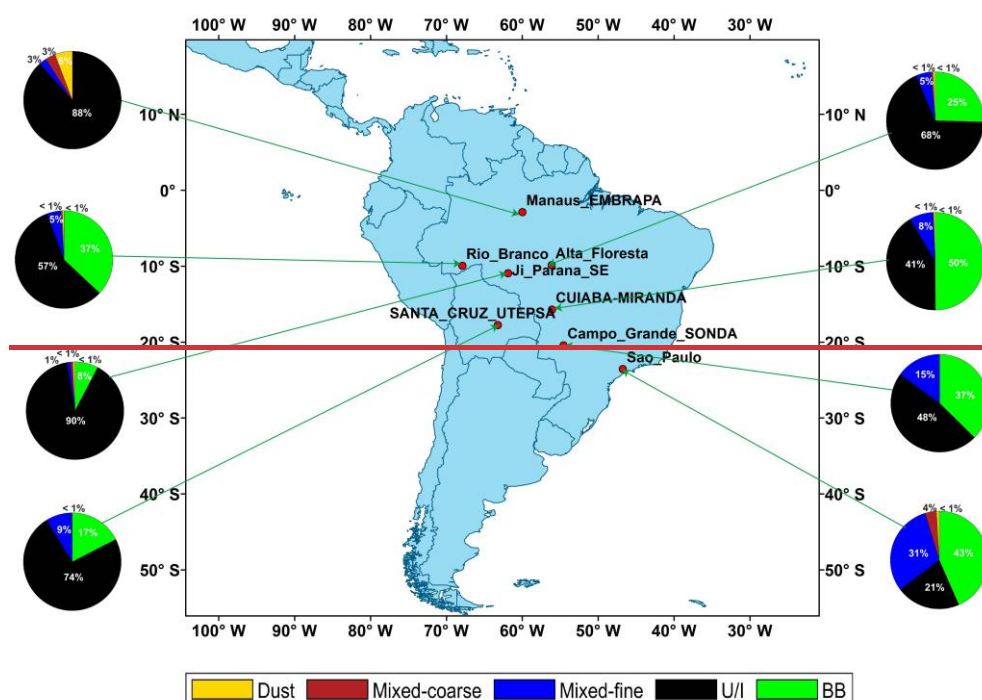
630 Figure 13 shows the aerosol types in Africa. Northern Africa has the largest desert  
 631 in the world, the Saharan Desert; therefore, dust aerosols dominate north of the  
 632 equator in Africa. However, some AERONET sites in the Sudanese steppe were  
 633 primarily BB, with some U/I aerosols in nearby urban sites. The Ilorin site is a typical  
 634 mixed aerosol site close to the equator with a small amount of BB aerosols. Most sites  
 635 close to the Atlantic coast were affected by dust aerosols, even those on the islands of  
 636 CapeCapo Verde. The reliability of the new model in distinguishing U/I and BB  
 637 aerosols is demonstrated. Sites in Southern Africa, such as Namibia, Botswana, and  
 638 Zambia, are dominated by BB aerosols. Nevertheless, studies have shown the  
 639 presence of U/I aerosols at sites in the urban areas of South Africa. Although U/I and  
 640 BB aerosols are difficult to distinguish, the two can be identified in the context of a  
 641 large urban population and less biomass combustion, thus establishing the model's  
 642 accuracy.



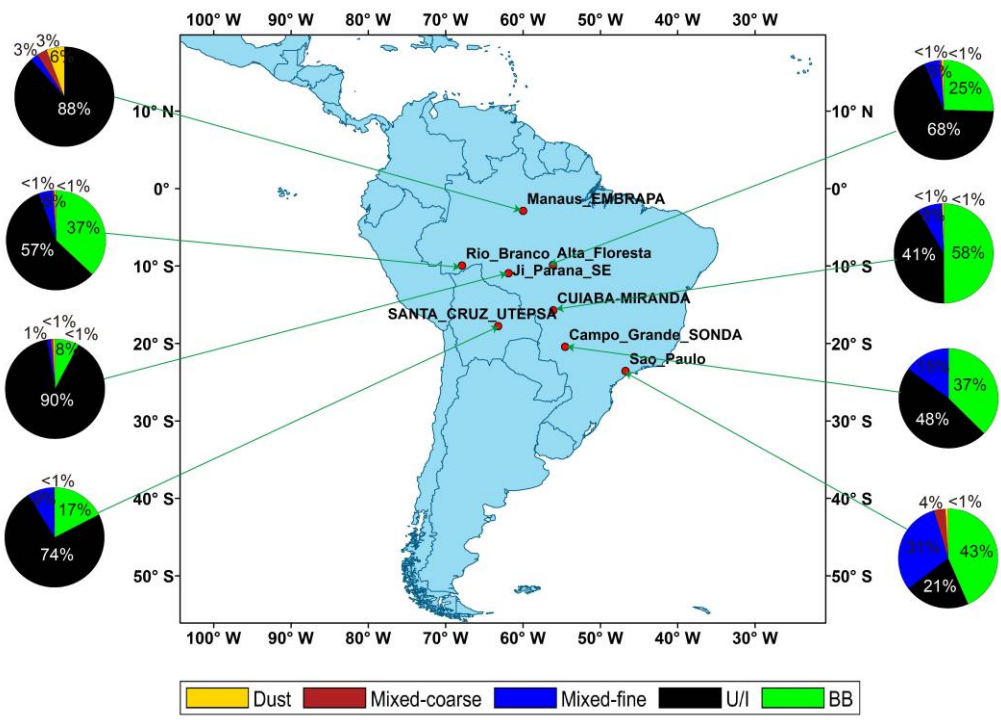
645 **Figure 13.** Same as Figure 12 but for Africa.

646 The aerosol types in South America are shown in Figure 14. Here, only eight sites

647 met the requirement for valid data >100 aerosol types. South America is mainly  
 648 dominated by mountainous plateaus, and under the influence of the Brazilian warm  
 649 current, many tropical rainforests are distributed in the south; therefore, the  
 650 background aerosols are mainly BB aerosols. As shown in Figure 14, large cities, such  
 651 as Rio Branco, Campo Grande, Manaus, Santa Cruz, and São Paulo, showed an  
 652 increased proportion of anthropogenic and mixed aerosols because of their large  
 653 population and developed industries. Due to the tropical rainforest climate in southern  
 654 South America, the proportion of BB aerosols increased, such as that at the Cuiaba  
 655 site near the Amazon River. Additionally, the Manaus site contained a small amount of  
 656 dust aerosols that were presumably transported across the Atlantic Ocean from  
 657 African dust at the same latitude.



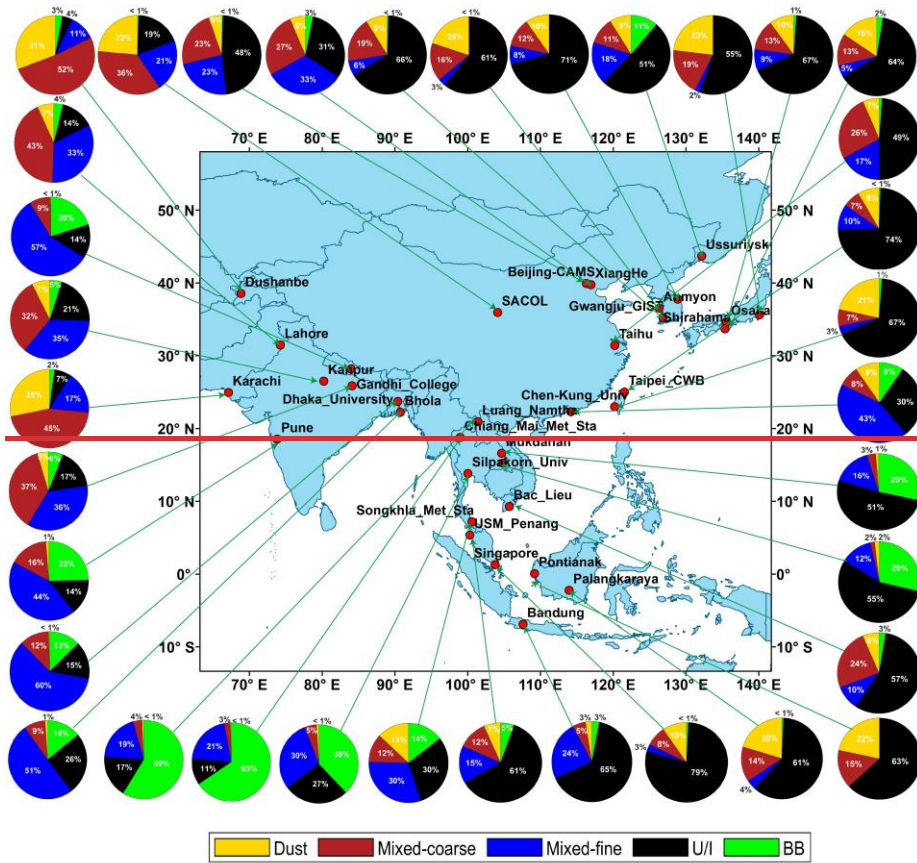
658



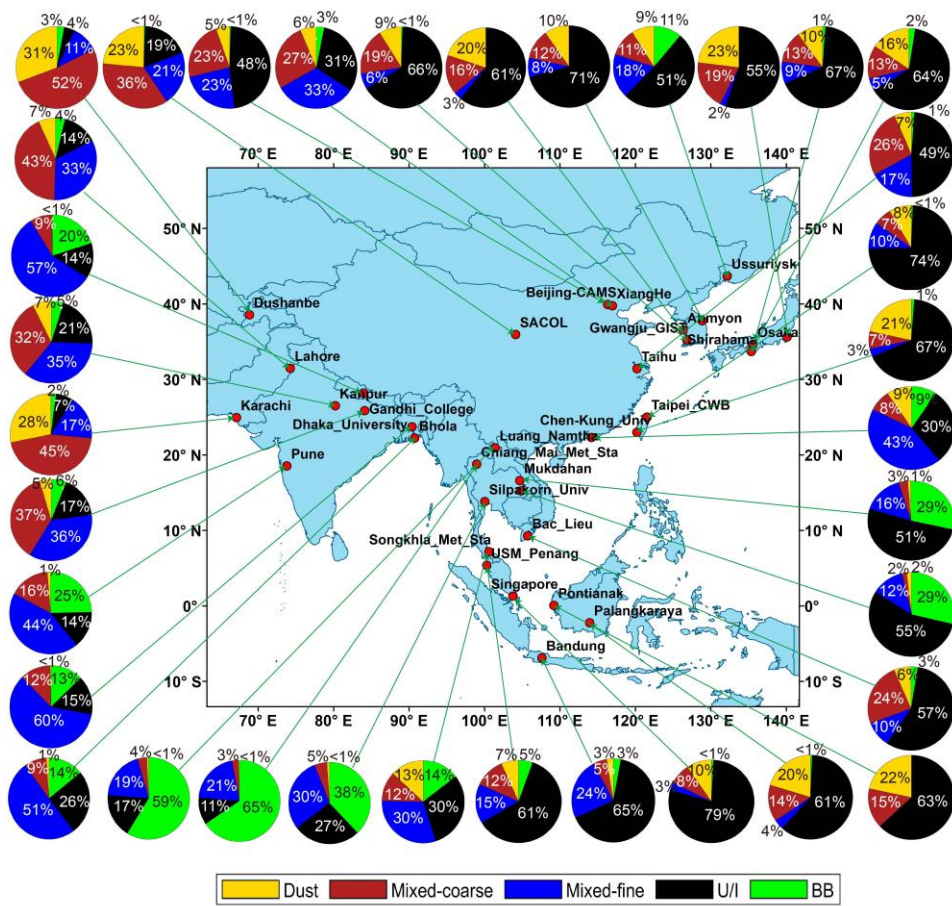
659

660 **Figure 14.** Same as Figure 12 but for South America.

661 The aerosol types in Asia are shown in Figure 15. In western Asia, influenced by  
 662 the Indian Desert, sites on the Indian Peninsula were dominated by coarse-particle  
 663 aerosols, including dust and mixed coarse aerosols. Kanpur and Pune are densely  
 664 populated cities in India, with more mixed-fine aerosols produced by human activities.  
 665 Additionally, in Southeast Asia, all sites contained BB aerosols, consistent with  
 666 Hamill (2014). This is because of the abundance of tropical rainforests in Southeast  
 667 Asia. Moreover, some urban sites, such as Singapore and Penang, had large numbers  
 668 of U/I and mixed-fine aerosols. The coastal areas of East Asia, which are densely  
 669 populated and industrially developed, were mainly dominated by U/I aerosols.  
 670 Moreover, dust aerosols appeared at these sites due to dust transported from the  
 671 Taklamakan Desert in East Asia.



672

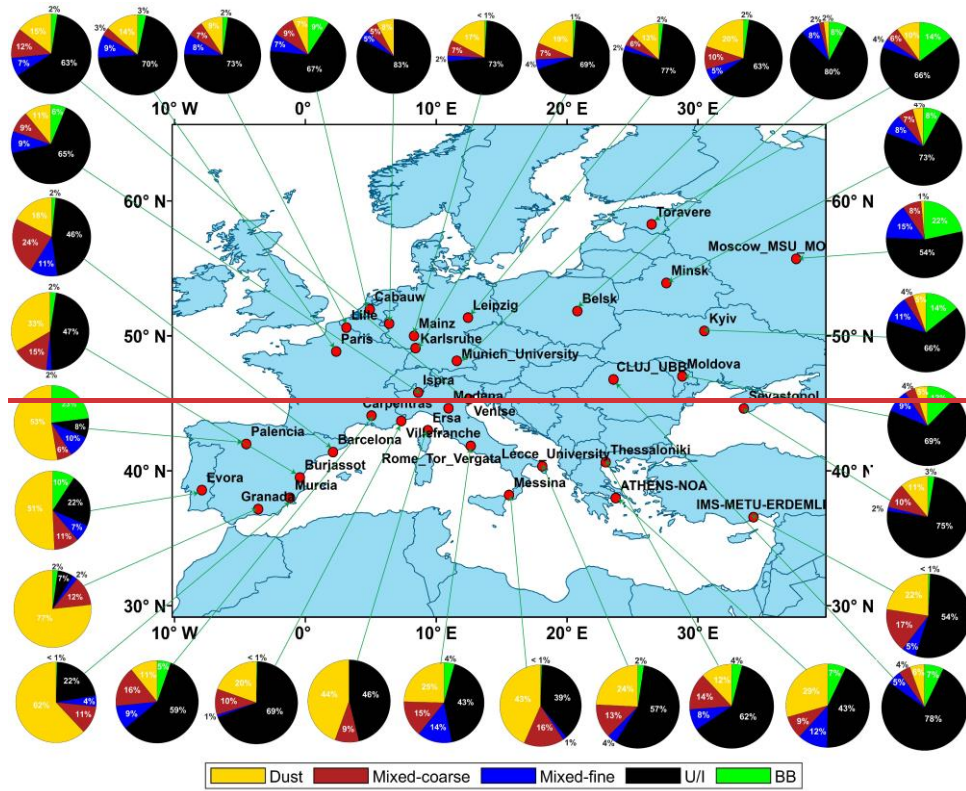


673

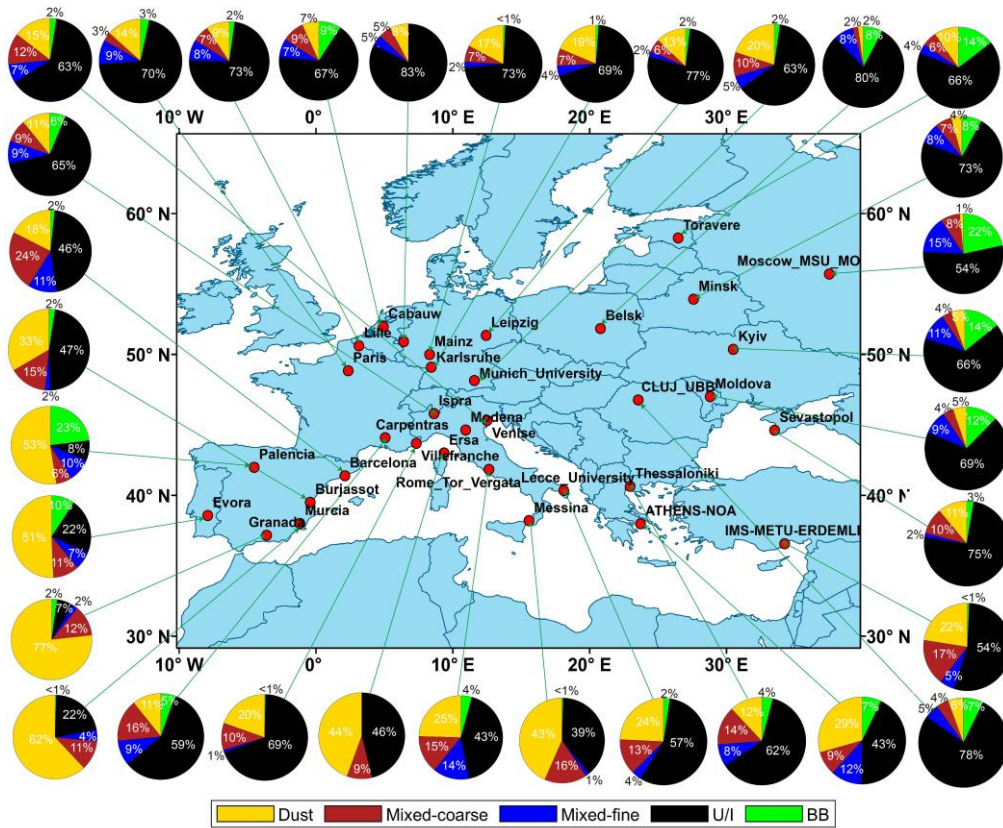
674 **Figure 15.** Same as Figure 12 but for Asia.

675 The inland areas of East Asia have a smaller population than the coastal areas;  
676 therefore, the proportion of U/I aerosols was small, and that of mixed aerosols was  
677 high. Generally, mixed aerosols are more easily overestimated than U/I aerosols;  
678 however, the new hybrid algorithm identified a larger proportion of U/I aerosols than  
679 mixed aerosols at Asian sites. Therefore, this new hybrid algorithm can be considered  
680 for improving the classification of mixed aerosols versus U/I aerosols.

681 Similarly, southern Europe, which is close to the Saharan and Arabian deserts,  
682 was dominated by dust aerosols, with small amounts of mixed and U/I aerosols.  
683 Northern European sites have many cities and a large population; therefore, the  
684 aerosol type was mainly U/I aerosols, identified using the new hybrid algorithm  
685 (Figure 16). Additionally, small amounts of BB aerosols were identified at most sites  
686 in Europe because of olive groves in agricultural lands in the EU, which produce 91%  
687 of the world's olive oil (Lopez-Pineiro et al., 2011). Papadakis et al. (2015) suggested  
688 that the biomass produced from olive oil is used for heating and industry, and its  
689 combustion produces carbonaceous aerosols, considered the major source of fine  
690 particle aerosols in Europe during winter (Puxbaum et al., 2007).

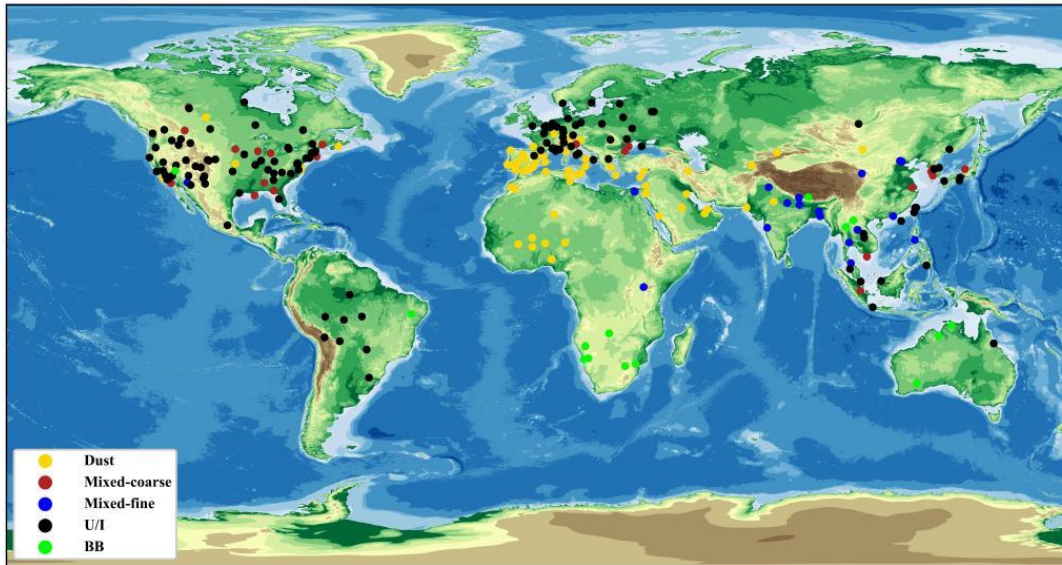


691



692

693 Figure 16. Same as Figure 12 but for Europe.



694

695 **Figure 17.** Global dominant aerosol types distribution based on AERONET sites.

696 The global distribution of dominant aerosols in the AERONET site is shown in  
 697 Figure 17. The graph does not include marine aerosols. There are more aerosol sites  
 698 on the global map than those on each continent because AERONET sites with > 5  
 699 years of data were selected for the global map; however, sites with > 100 valid data  
 700 points were required for each continent. The global distribution map shows that many  
 701 BB aerosols were distributed between 20°N and 20°S. This is because this region has  
 702 a predominantly tropical rainforest climate, with many tropical rainforests and more  
 703 carbon-containing aerosol emissions. This finding is consistent with those from  
 704 previous studies that found that global BB aerosols mainly originate from Africa  
 705 (approximately 52%), followed by South America (approximately 15%), equatorial  
 706 Asia (approximately 10%), boreal forests (approximately 9%), and Australia  
 707 (approximately 7%) (Van G. R. et al., 2010). Furthermore, the global distribution map  
 708 shows a clear distribution band of dust aerosols between 5°N and 35°N, originating  
 709 from the Saharan Desert in Africa and the Saudi Arabian Desert in Western Asia,  
 710 which are transported across the ocean to other regions.

## 711 **5. Conclusion**

712 We developed a new hybrid algorithm to support the rapid classification of



713 aerosol types by building an aerosol optical database for global AERONET sites. This  
714 hybrid algorithm is a complex aerosol-type processing algorithm that effectively  
715 integrates machine learning and density clustering algorithms. Additionally, this  
716 algorithm is not limited by the amount of data and improves the accuracy of aerosol-  
717 type classification. On investigating the aerosol types at specific sites with dominant  
718 aerosols, we observed that different sites contained one or more aerosol types, with  
719 the composition of some specific dominant aerosol sites being more complex than that  
720 of others. The new algorithm showed a higher accuracy than that shown by algorithms  
721 used in previous studies in identifying aerosol types at specific sites, particularly in  
722 distinguishing between U/I and mixed-fine aerosols. Finally, the recognition results of  
723 the new hybrid algorithm were closer to the baseline CRI, confirming that the new  
724 hybrid algorithm is better than the density-clustering algorithm. On investigating the  
725 aerosol types at global sites across the continents using the new algorithm, we  
726 observed the dominance of different types of aerosols at different sites, and the  
727 composition of these could be logically and effectively attributed to the geographical  
728 location, energy consumption structure, meteorological conditions and activities  
729 happening at the respective sites.

730 In this study, the existing aerosol type identification algorithm was improved  
731 using global ground-based AERONET optical property parameter data, and the spatial  
732 distribution characteristics of global aerosol types were analyzed, which impacted  
733 aerosol radiation research and optical thickness inversion accuracy. Additionally, the  
734 presumption of spherical dust aerosols in the Mie scattering model diverges from their  
735 actual non-spherical nature in the environment, introducing potential inaccuracies.  
736 The optical database's precision, therefore, necessitates further refinement. Future  
737 advancements could involve adopting more potent machine learning techniques, such  
738 as advanced algorithms beyond the current random forest method. Meanwhile, multi-  
739 source satellite data and reanalysis products can be incorporated into aerosol-type  
740 identification. Ultimately, this study will provide support for the identification and  
741 control of air pollution sources.

742 ~~In this study, the existing aerosol type identification algorithm was improved~~

743 ~~using global ground-based AERONET optical property parameter data, and the spatial~~  
744 ~~distribution characteristics of global aerosol types were analyzed, which impacted~~  
745 ~~aerosol radiation research and optical thickness inversion accuracy. However, marine~~

## 746 **Author contributions**

747 **Feng Zhang** designed the study. **Xiaoli Wei** analyzed the results, and wrote the  
748 original draft. **Qian Cui** engaged in data processing, manuscript editing, and  
749 restructuring. ~~**Qian Cui** collected and processed the data.~~ **Leiming Ma** revised the  
750 paper and given constructive suggestions. **Wenwen Li** constructive comments on the  
751 paper. **Peng Liu** revised the paper. All authors contributed to the study.

## 752 **Competing interests**

753 The authors declare that they have no conflict of interest.

## 754 **Acknowledgments**

755 This work was supported by the National Key R&D Program  
756 (2021YFB3900401), the National Natural Science Foundation of China (42105081  
757 and 42075125) and Science and Technology Foundation of Shanghai (23ZR1454100)

## 758 **References**

- 759 Van G. R., der W., Randerson, J. T., Giglio, L., Collatz, G. J., Mu, M., Kasibhatla, P. S., Morton, D. C.,  
760 Defries, R. S., Jin, Y., and Van Leeuwen, T. T.: Global fire emissions and the contribution of  
761 deforestation, savanna, forest, agricultural, and peat fires (1997–2009), Atmos. Chem. Phys., 10,  
762 11707–11735, <https://doi.org/10.5194/acp-10-11707-2010>, 2010.
- 763 Bahadur, R., Praveen, P. S., Xu, Y., and Ramanathan, V.: Solar absorption by elemental and brown  
764 carbon determined from spectral observations, Proc. Natl. Acad. Sci. U. S. A., 109, 17366–17371,  
765 <https://doi.org/10.1073/pnas.1205910109>, 2012.
- 766 Boselli, A., Caggiano, R., Cornacchia, C., Madonna, F., Mona, L., Macchiato, M., Pappalardo, G., and  
767 Trippetta, S.: Multi year sun-photometer measurements for aerosol characterization in a Central  
768 Mediterranean site, Atmos. Res., 104–105, 98–110, <https://doi.org/10.1016/j.atmosres.2011.08.002>,  
769 2012.
- 770 Breiman: Random forests, Machine Learning, 45(1), 5–32, <https://doi.org/10.1023/A:1010933404324>,  
771 2001.
- 772 Che, H., Bing, Q., Zhao, H., Xia, X., and Zhang, X.: Aerosol optical properties and direct radiative  
773 forcing based on measurements from the China Aerosol Remote Sensing Network (CARSNET) in  
774 eastern China, Atmos. Chem. Phys., 18, 405–425, <https://doi.org/10.5194/acp-18-405-2018>, 2018.

775 Choi, W., Lee, H., and Park, J.: A first approach to aerosol classification using space-borne  
776 measurement data: Machine learning-based algorithm and evaluation, *Remote Sens.*, 13, 1–21,  
777 <https://doi.org/10.3390/rs13040609>, 2021a.

778 Choi, W., Lee, H., Kim, D., and Kim, S.: Improving spatial coverage of satellite aerosol classification  
779 using a random forest model, *Remote Sens.*, 13 (7):1268. <https://doi.org/10.3390/rs13071268>, 2021b.

780 Dubovik, O. and King, M. D.: A flexible inversion algorithm for retrieval of aerosol optical properties  
781 from Sun and sky radiance measurements, *J. Geophys. Res. Atmos.*, 105, 20673–20696,  
782 <https://doi.org/10.1029/2000JD900282>, 2000.

783 Dubovik, O., Holben, B., Eck, T. F., Smirnov, A., Kaufman, Y. J., King, M. D., Tanré, D., and Slutsker,  
784 I.: Variability of absorption and optical properties of key aerosol types observed in worldwide  
785 locations, *J. Atmos. Sci.*, 59, 590–608, <https://doi.org/10.1175/1520-0469>, 2002.

786 Eck, T. F., Holben, B. N., Reid, J. S., Dubovik, O., Smirnov, A., O’Neill, N. T., Slutsker, I., and Kinne,  
787 S.: Wavelength dependence of the optical depth of biomass burning, urban, and desert dust aerosols,  
788 *J. Geophys. Res. Atmos.*, 104, 31333–31349, <https://doi.org/10.1029/1999JD900923>, 1999.

789 [Elham Ghasemifar: Climatology of aerosol types and their vertical distribution over Iran using  
790 CALIOP dataset during 2007–2021. \*Remote Sensing Applications: Society and Environment\*. 32,  
791 101053, 2352–9385. <https://doi.org/10.1016/j.rsase.2023.101053>. 2023.](https://doi.org/10.1016/j.rsase.2023.101053)

792 Fernandez-Delgado, M., Cernadas, E., Barro, S., and Amorim, D.: Do we Need Hundreds of Classifiers  
793 to Solve Real World Classification Problems?, *J. Mach. Learn. Res.*, 15, 3133–3181,  
794 <https://dl.acm.org/doi/10.5555/2627435.2697065>, 2014.

795 Giles, D. M., Holben, B. N., Eck, T. F., Sinyuk, A., Smirnov, A., Slutsker, I., Dickerson, R. R.,  
796 Thompson, A. M., and Schafer, J. S.: An analysis of AERONET aerosol absorption properties and  
797 classifications representative of aerosol source regions, *J. Geophys. Res. Atmos.*, 117, 1–16,  
798 <https://doi.org/10.1029/2012JD018127>, 2012.

799 Hamill, P., Giordano, M., Ward, C., Giles, D., and Holben, B.: An AERONET-based aerosol  
800 classification using the Mahalanobis distance, *Atmos. Environ.*, 140, 213–233,  
801 <https://doi.org/10.1016/j.atmosenv.2016.06.002>, 2016.

802 Hess, M., Koepke, P., and Schult, I.: Optical properties of Aerosols and Clouds: The Software Package  
803 OPAC, *Bull. Am. Meteorol. Soc.*, 79, 831–844, [https://doi.org/10.1175/1520-0477\(1998\)079<0831:OPOAAC>2.0.CO;2](https://doi.org/10.1175/1520-0477(1998)079<0831:OPOAAC>2.0.CO;2), 1998.

804 Kalapureddy, M. C. R., Kaskaoutis, D. G., Ernest Raj, P., Devara, P. C. S., Kambezidis, H. D.,  
805 Kosmopoulos, P. G., and Nastos, P. T.: Identification of aerosol type over the Arabian Sea in the  
806 premonsoon season during the Integrated Campaign for Aerosols, Gases and Radiation Budget  
807 (ICARB), *J. Geophys. Res. Atmos.*, 114, 1–12, <https://doi.org/10.1029/2009JD011826>, 2009.

808 Kaskaoutis, D. G., Kharol, S. K., Sinha, P. R., Singh, R. P., Badarinath, K., Mehdi, W., and Sharma, M.:  
809 Contrasting aerosol trends over South Asia during the last decade based on MODIS observations,  
810 *Atmos. Meas. Tech. Discuss.*, 4, 5275–5323, <https://doi.org/10.5194/amtd-4-5275-2011>, 2011.

811 Kiehl, J. T. and Briegleb, B. P.: The relative roles of sulfate aerosols and greenhouse gases in climate  
812 forcing, *Science (80-. )*, 260, 311–314, <http://dx.doi.org/10.1126/science.260.5106.311>, 1993.

813 Kim, J., Lee, J., Lee, H. C., Higurashi, A., Takemura, T., and Song, C. H.: Consistency of the aerosol  
814 type classification from satellite remote sensing during the Atmospheric Brown Cloud-East Asia  
815 Regional Experiment campaign, *J. Geophys. Res. Atmos.*, 112, 1–12,  
816 <https://doi.org/10.1029/2006JD008201>, 2007.

817 Kumar, K. R., Kang, N., and Yin, Y.: Classification of key aerosol types and their frequency  
818

819 distributions based on satellite remote sensing data at an industrially polluted city in the Yangtze  
820 River Delta, China, *Int. J. Climatol.*, 38, 320–336, <https://doi.org/10.1002/joc.5178>, 2018.

821 Lee, J., Kim, J., Song, C. H., Kim, S. B., Chun, Y., Sohn, B. J., and Holben, B. N.: Characteristics of  
822 aerosol types from AERONET sunphotometer measurements, *Atmos. Environ.*, 44, 3110–3117,  
823 <https://doi.org/10.1016/j.atmosenv.2010.05.035>, 2010.

824 Levy, R. C., Remer, L. A., Mattoo, S., Vermote, E. F., and Kaufman, Y. J.: Second-generation  
825 operational algorithm: Retrieval of aerosol properties over land from inversion of Moderate  
826 Resolution Imaging Spectroradiometer spectral reflectance, *J. Geophys. Res. Atmos.*, 112,  
827 <https://doi.org/10.1029/2006JD007811>, 2007.

828 Li, K., Bai, K., Ma, M., Guo, J., Li, Z., Wang, G., and Chang, N. Bin: Spatially gap free analysis of  
829 aerosol type grids in China: First retrieval via satellite remote sensing and big data analytics, *ISPRS  
830 J. Photogramm. Remote Sens.*, 193, 45–59, <https://doi.org/10.1016/j.isprsjprs.2022.09.001>, 2022.

831 Lin, J., Zheng, Y., Shen, X., Xing, L., and Che, H.: Global aerosol classification based on aerosol  
832 robotic network (Aeronet) and satellite observation, *Remote Sens.*, 13, 1–23,  
833 <https://doi.org/10.3390/rs13061114>, 2021.

834 Lopez-Pineiro, A., Cabrera, D., Albarran, A., and Pefia, D.: Influence of two-phase olive mill waste  
835 application to soil on terbuthylazine behaviour and persistence under controlled and field conditions,  
836 *J. Soils Sediments*, 11, 771–782, <https://doi.org/10.1007/s11368-011-0362-3>, 2011.

837 Lu, F., Chen, S., Hu, Z., Han, Z., Alam, K., Luo, H., Bi, H., Chen, J., and Guo, X.: Sensitivity and  
838 uncertainties assessment in radiative forcing due to aerosol optical properties in diverse locations in  
839 China, *Sci. Total Environ.*, 860, 160447, <https://doi.org/10.1016/j.scitotenv.2022.160447>, 2023.

840 Michael, I., Mishchenko, and, Larry, D., and Travis: Light scattering by polydisperse, rotationally  
841 symmetric nonspherical particles: Linear polarization, *J. Quant. Spectrosc. Radiat. Transf.*,  
842 [https://doi.org/10.1016/0022-4073\(94\)90130-9](https://doi.org/10.1016/0022-4073(94)90130-9), 1994.

843 Moraes, C. P. A., Fantinato, D. G., and Neves, A.: Epanechnikov kernel for PDF estimation applied to  
844 equalization and blind source separation, *Signal Processing*, 189, 108251,  
845 <https://doi.org/10.1016/j.sigpro.2021.108251>, 2021.

846 [Nandan, R., Ratnam, M.V., Kiran, V.R., Madhavan, B.L., & Naik, D.N.: Estimation of Aerosol  
847 Complex Refractive Index over a tropical atmosphere using a synergy of in-situ measurements.  
848 Atmospheric Research, 257, 105625, https://doi.org/10.1016/J.ATMOSRES.2021.105625, 2021](#)

849 Nicolae, D., Vasilescu, J., Talianu, C., Binietoglou, I., Nicolae, V., Andrei, S., and Antonescu, B.: A  
850 neural network aerosol-typing algorithm based on lidar data, *Atmos. Chem. Phys.*, 18, 14511–14537,  
851 <https://doi.org/10.5194/acp-18-14511-2018>, 2018.

852 Omar, A. H., Won, J. G., Winker, D. M., Yoon, S. C., Dubovik, O., and McCormick, M. P.:  
853 Development of global aerosol models using cluster analysis of Aerosol Robotic Network  
854 (AERONET) measurements, *J. Geophys. Res. D Atmos.*, 110, 1–14,  
855 <https://doi.org/10.1029/2004JD004874>, 2005.

856 Pace, G., di Sarra, A., Meloni, D., Piacentino, S., and Chamard, P.: Aerosol optical properties at  
857 Lampedusa (Central Mediterranean). 1. Influence of transport and identification of different aerosol  
858 types, *Atmos. Chem. Phys.*, 6, 697–713, <https://doi.org/10.5194/acp-6-697-2006>, 2006.

859 Papadakis, G. Z., Megaritis, A. G., and Pandis, S. N.: Effects of olive tree branches burning emissions  
860 on PM<sub>2.5</sub> concentrations, *Atmos. Environ.*, 112, 148–158,  
861 <https://doi.org/10.1016/j.atmosenv.2015.04.014>, 2015.

862 Pathak, B., Bhuyan, P. K., Gogoi, M., and Bhuyan, K.: Seasonal heterogeneity in aerosol types over

863 Dibrugarh-North-Eastern India, *Atmos. Environ.*, 47, 307–315,  
864 <https://doi.org/10.1016/j.atmosenv.2011.10.061>, 2012.

865 Pawar, G. V., Devara, P. C. S., and Aher, G. R.: Identification of aerosol types over an urban site based  
866 on air-mass trajectory classification, *Atmos. Res.*, 164–165, 142–155,  
867 <https://doi.org/10.1016/j.atmosres.2015.04.022>, 2015.

868 Puxbaum, H., Caseiro, A., Sánchez-Ochoa, A., Kasper-Giebl, A., Claeys, M., Gelencsér, A., Legrand,  
869 M., Preunkert, S., and Pio, C.: Levoglucosan levels at background sites in Europe for assessing the  
870 impact of biomass combustion on the European aerosol background, *J. Geophys. Res.*, 112, D23S05,  
871 <https://doi.org/10.1029/2006JD008114>, 2007.

872 Ramanathan, V., Crutzen, P. J., Lelieveld, J., Mitra, A. P., Althausen, D., Anderson, J., Andreae, M. O.,  
873 Cantrell, W., Cass, G. R., and Chung, C. E.: Indian Ocean Experiment: An integrated analysis of the  
874 climate forcing and effects of the great Indo-Asian haze, *J. Geophys. Res. Atmos.*, 106,  
875 <https://doi.org/10.1029/2001JD900133>, 2001.

876 Raut, J. C. and Chazette, P.: Radiative budget in the presence of multi-layered aerosol structures in the  
877 framework of AMMA SOP-0, *Atmos. Chem. Phys.*, 8, 6839–6864, [https://doi.org/10.5194/acp-8-](https://doi.org/10.5194/acp-8-6839-2008)  
878 [6839-2008](https://doi.org/10.5194/acp-8-6839-2008), 2008.

879 [Reddy LA, Glover TA, Dudek CM, Alperin A, Wiggs NB, Bronstein B.: A randomized trial examining](https://doi.org/10.1016/j.jsp.2022.04.002)  
880 [the effects of paraprofessional behavior support coaching for elementary students with disruptive](https://doi.org/10.1016/j.jsp.2022.04.002)  
881 [behavior disorders: Paraprofessional and student outcomes. \*J Sch Psychol.\* 2022 Jun;92:227-245.](https://doi.org/10.1016/j.jsp.2022.04.002)  
882 <https://doi.org/10.1016/j.jsp.2022.04.002>, 2022.

883 Redemann, J., Turco, R. P., Liou, K. N., Russell, P. B., Bergstrom, R. W., Schmid, B., Hobbs, P. V,  
884 Hartley, W. S., Ismail, S., and Ferrare, R. A.: Retrieving the vertical structure of the effective aerosol  
885 complex index of refraction from a combination of aerosol in situ and remote sensing measurements  
886 during TARFOX, *J. Geophys. Res.*, 105( D8), 9949– 9970, doi:10.1029/1999JD901044,2000.

887 Remer, L. A., Tanré, D., and Kaufman, Y. J.: Algorithm for remote sensing of tropospheric aerosol from  
888 MODIS: Collection 005, 2009.

889 Rosenblatt, M.: Remarks on Some Nonparametric Estimates of a Density Function, Remarks on Some  
890 Nonparametric Estimates of a Density Function. In: Davis, R., Lii, KS., Politis, D. (eds) Selected  
891 Works of Murray Rosenblatt. Selected Works in Probability and Statistics. Springer, New York, NY.  
892 [https://doi.org/10.1007/978-1-4419-8339-8\\_13](https://doi.org/10.1007/978-1-4419-8339-8_13), 2011.

893 Sheridan, P. J., Delene, D. J., and Ogren, J. A.: Four Years of Continuous Surface Aerosol  
894 Measurements from the DOE / ARM Southern Great Plains CART Site, 1–8,  
895 <https://doi.org/10.1029/2001JD000785>, 2001.

896 Shin, S. K., Tesche, M., Noh, Y., and Müller, D.: Aerosol-type classification based on AERONET  
897 version 3 inversion products, *Atmos. Meas. Tech.*, 12, 3789–3803, [https://doi.org/10.5194/amt-12-](https://doi.org/10.5194/amt-12-3789-2019)  
898 [3789-2019](https://doi.org/10.5194/amt-12-3789-2019), 2019.

899 Siomos, N., Fountoulakis, I., Natsis, A., Drosoglou, T., and Bais, A.: Automated aerosol classification  
900 from spectral UV measurements using machine learning clustering, *Remote Sens.*, 12, 1–18,  
901 <https://doi.org/10.3390/rs12060965>, 2020.

902 Tanré, D., Kaufman, Y. J., Holben, B. N., Chatenet, B., Karnieli, A., Lavenu, F., Blarel, L., Dubovik, O.,  
903 Remer, L. A., and Smirnov, A.: Climatology of dust aerosol size distribution and optical properties  
904 derived from remotely sensed data in the solar spectrum, *J. Geophys. Res. Atmos.*, 106, 18205–  
905 18217, <https://doi.org/10.1029/2000JD900663>, 2001.

906 Tong, H., Lakey, P. S. J., Arangio, A. M., Socorro, J., Kampf, C. J., Berkemeier, T., Brune, W. H.,

907 Pöschl, U., and Shiraiwa, M.: Reactive oxygen species formed in aqueous mixtures of secondary  
908 organic aerosols and mineral dust influencing cloud chemistry and public health in the Anthropocene,  
909 Faraday Discuss., 200, 251–270, <https://doi.org/10.1039/c7fd00023e>, 2017.

910 [Wang J, Liu Y, Chen L, Liu Y, Mi K, Gao S, Mao J, Zhang H, Sun Y, Ma Z.: Validation and calibration](#)  
911 [of aerosol optical depth and classification of aerosol types based on multi-source data over China.](#)  
912 [Sci Total Environ. 2023 Dec 10;903:166603. doi: 10.1016/j.scitotenv.2023.](#)

913 Wu, Y., Li, J., Xia, Y., Deng, Z., Tao, J., Tian, P., Gao, Z., Xia, X., and Zhang, R.: Size-resolved  
914 refractive index of scattering aerosols in urban Beijing: A seasonal comparison, Aerosol Sci.  
915 Technol., 55, 1070–1083, <https://doi.org/10.1080/02786826.2021.1924357>, 2021.

916 Yang, M., Howell, S. G., Zhuang, J., and Huebert, B. J.: Attribution of aerosol light absorption to black  
917 carbon, brown carbon, and dust in China - Interpretations of atmospheric measurements during  
918 EAST-AIRE, Atmos. Chem. Phys., 9, 2035–2050, <https://doi.org/10.5194/acp-9-2035-2009>, 2009.

919 Yokelson, R. J., Urbanski, S. P., Atlas, E. L., Toohey, D. W., Alvarado, E. C., Crouse, J. D., Wennberg,  
920 P. O., Fisher, M. E., Wold, C. E., and Campos, T. L.: Emissions from forest fires near Mexico City ,  
921 Atmos. Chem. Phys., 7, 5569–5584, <https://doi.org/10.5194/acp-7-5569-2007>, 2007.

922 Yousefi, R., Wang, F., Ge, Q., and Shaheen, A.: Long-term aerosol optical depth trend over Iran and  
923 identification of dominant aerosol types, Sci. Total Environ., 722,  
924 <https://doi.org/10.1016/j.scitotenv.2020.137906>, 2020.

925 Zhang, L. and Li, J.: Variability of major aerosol types in China classified using AERONET  
926 measurements, Remote Sens., 11, <https://doi.org/10.3390/rs11202334>, 2019.

927